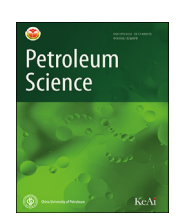
KeAi
CHINESE ROOTS
GLOBAL IMPACT

Contents lists available at ScienceDirect

Petroleum Science

journal homepage: www.keaipublishing.com/en/journals/petroleum-science



Original Paper

CO₂-EOR microscopic mechanism under injection—production coupling technology in low-permeability reservoirs



Zheng Chen ^{a, b}, Yu-Liang Su ^{a, b, *}, Lei Li ^{a, b}, Yong-Mao Hao ^{a, b}, Wen-Dong Wang ^{a, b}, Chui-Xian Kong ^c

- ^a Key Laboratory of Unconventional Oil & Gas Development (China University of Petroleum (East China)), Ministry of Education, Qingdao, 266580, Shandong, PR China
- ^b School of Petroleum Engineering, China University of Petroleum (East China), Qingdao, 266580, Shandong, PR China
- ^c Research Institute of Exploration and Development, Xinjiang Oilfield Company, Karamay, 834000, Xinjiang, PR China

ARTICLE INFO

Article history: Received 15 May 2024 Received in revised form 2 November 2024 Accepted 6 November 2024 Available online 7 November 2024

Edited by Yan-Hua Sun

Keywords:
Low-permeability reservoirs
Injection—production coupling
Microscopic experimental simulation
technology
CO₂-EOR
Mechanical analysis

ABSTRACT

Injection-production coupling (IPC) technology holds substantial potential for boosting oil recovery and enhancing economic efficiency. Despite this potential, discussion on gas injection coupling, especially in relation to microscopic mechanisms, remains relatively sparse. This study utilizes microscopic visualization experiments to investigate the mechanisms of residual oil mobilization under various IPC scenarios, complemented by mechanical analysis at different stages. The research quantitatively assesses the degree of microscopic oil recovery and the distribution of residual oil across different injection -production methods. Findings reveal that during the initial phase of continuous gas injection (CGI), the process closely mimics miscible displacement, gradually transitioning to immiscible displacement as CO₂ extraction progresses. Compared to CGI, the asynchronous injection-production (AIP) method improved the microscopic oil recovery rate by 6.58%. This enhancement is mainly attributed to significant variations in the pressure field in the AIP method, which facilitate the mobilization of columnar and porous residual oil. Furthermore, the synchronous cycle injection (SCI) method increased microscopic oil recovery by 13.77% and 7.19% compared to CGI and AIP, respectively. In the SCI method, membrane oil displays filamentary and Kármán vortex street flow patterns. The dissolved and expanded crude oil tends to accumulate and grow at the oil-solid interface due to adhesive forces, thereby reducing migration resistance. The study findings provide a theoretical foundation for improving oil recovery in lowpermeability reservoirs.

© 2024 The Authors. Publishing services by Elsevier B.V. on behalf of KeAi Communications Co. Ltd. This is an open access article under the CC BY license (http://creativecommons.org/licenses/by/4.0/).

1. Introduction

As global attention on carbon reduction targets intensifies, the application of CO₂-enhanced oil recovery (EOR) technology in reservoir development has garnered widespread interest (AL-khulaidi et al., 2024; Li, 2023; Menefee and Ellis, 2020). This is particularly true for low-permeability reservoirs, where the dual potential of improving oil recovery and achieving carbon sequestration makes it a key technology in addressing climate change and meeting energy demands (Jiang et al., 2022; Kumar et al., 2023). Low-permeability reservoirs, with their complex pore structures and limited fluid displacement capacity, often render traditional

* Corresponding author.

E-mail address: suyuliang@upc.edu.cn (Y.-L. Su).

production enhancement techniques ineffective (Liu et al., 2024). Therefore, studying the microscopic displacement behavior and storage mechanisms of CO₂ in low-permeability reservoirs, particularly under injection—production coupling (IPC) technology, is crucial for efficient reservoir development and carbon reduction (Askarova et al., 2023; Liu et al., 2022; Yu et al., 2024).

In recent years, research has shown that CO₂-EOR technology has yielded promising results in improving the extraction efficiency of low-permeability reservoirs and enhancing CO₂ sequestration capabilities (Huang et al., 2016; Kang et al., 2022; Song et al., 2018a; Wei et al., 2021). Many scholars have conducted targeted studies of the enhanced oil recovery mechanisms of CO₂ at the micro and nanoscale (Davoodi et al., 2022; Li et al., 2021b; Zhang et al., 2019). The miscibility and pore size significantly affect subsurface fluid flow characteristics (Chen et al., 2022a). Against this backdrop, Li et al. (2023b) conducted microfluidic experiments to study the

dynamic interfacial behavior between oil and gas under different temperature and pressure conditions and the degree of microscopic recovery in blind-end pores of varying sizes, including the impact of surfactants. Lu et al. (2021) used particle image velocimetry and fluorescence visualization techniques to monitor the behavior of oil-gas-water phases and multiphase flow under reservoir conditions, revealing the mobilization of the oil phase during CO₂ huffand-puff under different wettability conditions (Oian et al., 2018). Additionally, scanning electron microscopy (SEM) and X-ray diffraction (XRD) experiments can further enhance our understanding of the interactions between CO₂ and rock (Khather et al., 2019; Zhang et al., 2022b). In the studies mentioned above, researchers predominantly used regular pore-throat structures, whereas actual subsurface rock structures are often far more complex (Hou et al., 2023; Sadeghnejad et al., 2021). Currently, scholars primarily use CT scans and SEM experiments on reservoir cores to obtain the true pore structures of specific subsurface reservoir regions (Cui et al., 2017; Wang et al., 2020). Using microfluidic experimental equipment, the microscopic flow characteristics and residual oil distribution of oil-gas-water in real subsurface porous media can be studied (Tang et al., 2023; Zhu et al., 2024). Quantitative analysis was conducted on gas microscopic sweep efficiency, recovery rate, and residual oil distribution. Additionally, the influence of fracture-matrix structure and wettability on fluid-solid interaction mechanisms and CO₂ miscible interface behavior mechanisms was also discussed (Li et al., 2024). In heavy and deep oil reservoirs, interactions between CO₂ and crude oil under specific temperature and pressure conditions can lead to the deposition of heavy components like asphaltenes, which can damage reservoir properties (Mahdavi et al., 2024; Syed et al., 2020). Some researchers have studied this phenomenon at the microscale, identifying changes in particle size under varying pressures and CO2 concentrations (Song et al., 2018b), and quantitatively characterizing the extent of reservoir property damage caused by heavy component deposition (Zhang et al., 2022a). On the other hand, the strong heterogeneity of reservoirs can create preferential CO₂ channels, which may impact the effectiveness of CO₂-EOR (Luo et al., 2022; Wang et al., 2023). To address this issue, Chen et al. (2024) studied the microscopic migration behavior and interaction mechanisms of CO2 in heterogeneous reservoirs with preferential channels, elucidating the microscale mechanisms of CO₂-EOR in such reservoirs (Guo et al., 2022; Lv et al., 2022). There are currently various CO₂-EOR technologies, with injection strategy optimization being a crucial component (Dudek et al., 2021). This method has shown significant improvements in both oil recovery and CO₂ sequestration efficiency (Ahmadi et al., 2016; Syah et al., 2021). The optimization of CO₂ injection strategies primarily focuses on injection methods (Li et al., 2023a; Yao et al., 2023), including continuous CO₂ injection, wateralternating-gas (WAG) injection, carbonated water injection, and CO₂-CH₄ WAG (Cho et al., 2021; Li et al., 2021a; Yu et al., 2021). Additionally, the injection-production layers for CO2 have also been optimized (Alam et al., 2022). Injection-production coupling technology is a production enhancement method that alternates between injection and production wells to increase the sweep efficiency of injected fluids in the reservoir (Wang et al., 2018). This technique involves adjustments to the operational regime within injection strategies. Currently, injection-production coupling has been applied in water injection (Wang et al., 2018), polymer injection (Li et al., 2019), and CO₂ injection (Zheng et al., 2021). In CO₂ injection-production coupling, Sun et al. (2023) studied the migration of the miscible front in tight reservoirs and found that injection-production coupling can mitigate CO₂ breakthrough to some extent. Additionally, Chen et al. (2022b) evaluated the effectiveness of injection—production coupling through

experiments, showing that this technique can increase oil recovery to some extent. Table 1 presents the current research on CO₂-EOR by various scholars and the associated challenges.

As shown in Table 1, most scholars employ experimental methods to investigate CO₂-EOR effects and sequestration mechanisms, while theoretical simulations are less frequently used. Research on enhanced oil recovery mechanisms and the effects of injection—production coupling technology has primarily been conducted at the macroscopic level, with limited exploration into gas injection coupling. Although there have been some advances in understanding CO2 microscale flow and enhanced recovery mechanisms, research on microscale oil displacement mechanisms during gas injection coupling remains insufficient. To address this gap, this study designs experimental methods for injection-production coupling using microfluidic techniques. The study begins by analyzing the distribution and mobilization of residual oil during continuous gas injection (CGI), followed by asynchronous injection-production (AIP) experiments based on CGI. It examines residual oil distribution and microscale recovery under both coupling methods, detailing the mobilization processes of membrane, columnar, and porous oil during AIP. Finally, synchronized cycle injection (SCI) experiments are conducted to investigate the mobilization mechanisms and distribution states of residual oil. The study also explores the mechanical mechanisms involved in residual oil mobilization across different methods, shedding light on the activation mechanisms of residual oil in various states. These findings offer theoretical insights into enhancing CO2 utilization efficiency and storage mechanisms through injection-production coupling technology.

2. Experiment and materials

2.1. Microscale simulation model preparation

Core samples provide the most accurate geological data for reflecting reservoir pore-throat characteristics. Fig. 1 illustrates the preparation process of the microscopic simulation model. The core samples used in this study were obtained from the G block of Shengli Oilfield, China. The reservoir has a top depth of 2950 m, an effective thickness of 20.5 m, permeability ranging from 0.077 to 23.8 mD, and porosity between 5.1% and 18.5%. The original reservoir pressure was 42.6 MPa (Li et al., 2016), but due to recent development, the current pressure has decreased to 20 MPa. In actual production, the block utilizes a typical five-spot well pattern with one injection well and four production wells, and CO₂ is used as the injection gas. This block is a typical low-permeability reservoir where CO2 is used for enhanced oil recovery. Therefore, this study selected actual geological cores from this reservoir for casting thin-section experiments, with the scanned images of the thin sections shown in Fig. 1(a). Secondly, the pore-throat structure within the core sample was identified, and the characteristics of the target reservoir pores were determined. Through preprocessing, analysis, restoration, and correction of the reservoir morphology, an equivalent diagram of the pore-throat structure suitable for microscopic visualization experiments was extracted (Fig. 1(b)). A laser etching device was then used to engrave the characteristic images of typical reservoir rock pore-throat structures, while fluid inlet and outlet channels were simultaneously drilled into glass plates. Finally, the two glass plates were fused together using a thermal fusion device under high-temperature conditions. The resulting microscopic model is shown in Fig. 1(c), with the distribution of etched pore-throats illustrated in Fig. 1(d).

By analyzing the pores in the scanned thin sections (Fig. 1(a)), the pore size distribution of the rock samples was measured, ranging from 20 to 187 μ m, with an average of approximately

Table 1 Summary of CO₂-EOR technology research.

| Reference | Research method | Research factor | Micro-pore scale | Actual porous media | IPC |
|----------------------|-----------------------------|-------------------------------------|------------------|---------------------|-----|
| Li et al. (2023b) | Experimental | Temperature and pressure conditions | Yes | No | No |
| Lu et al. (2021) | Experimental | Wettability conditions | Yes | No | No |
| Wang et al. (2020) | Experimental | Injection mode | Yes | Yes | No |
| Cui et al. (2017) | Experimental | Water cut | Yes | Yes | No |
| Zhu et al. (2024) | Experimental | Injection mode | Yes | Yes | No |
| Tang et al. (2023) | Experimental | Pore structure | Yes | Yes | No |
| Song et al. (2018b) | Experimental | Temperature and pressure conditions | Yes | Yes | No |
| Zhang et al. (2022a) | Experimental | Injection mode | Yes | Yes | No |
| Chen et al. (2024) | Experimental | Injection-production method | Yes | Yes | Yes |
| Guo et al. (2022) | Experimental | Injection mode | Yes | No | No |
| Syah et al. (2021) | Experimental | Injection mode | No | No | No |
| Wei et al. (2021) | Experimental and simulation | WAG and SAG | No | No | No |
| Ahmadi et al. (2016) | Numerical simulation | Injection mode | No | No | No |
| Yao et al. (2023) | Numerical simulation | Multi-phase strategy | No | No | No |
| Li et al. (2023a) | Experimental | Injection strategies | No | No | No |
| Cho et al. (2021) | Numerical simulation | Injection medium | No | No | No |
| Yu et al. (2021) | Experimental | Injection mode | No | No | No |
| Chen et al. (2022b) | Experimental | Injection parameters | No | No | No |
| Li et al. (2021a) | Experimental | Injection strategies | No | No | No |
| This work | Experimental | Injection—production method | Yes | Yes | Yes |

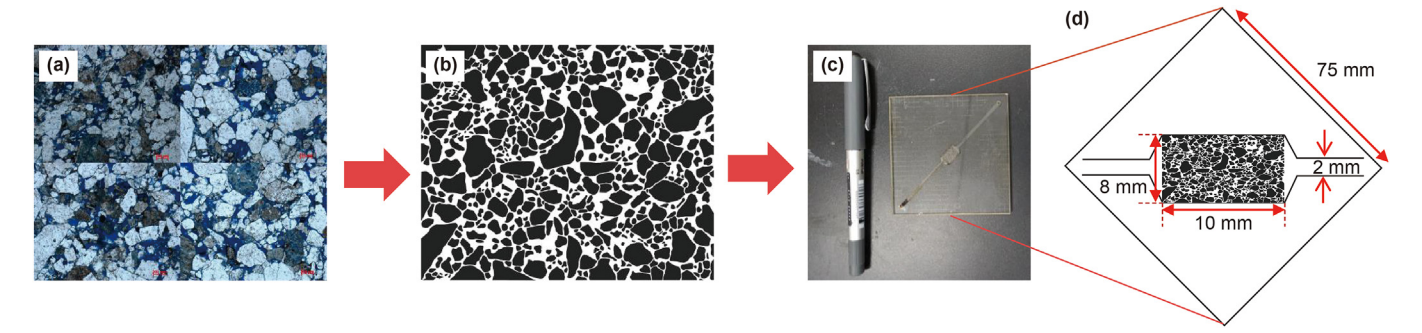


Fig. 1. The preparation process of the microsimulation model: (a) scanned image of the cast thin section, (b) equivalent diagram of pore-throat structure, (c) microscopic model prototype, (d) internal pore-throat structure of the microscopic model.

71.6 μm . The etched two-dimensional glass microscopic model in this study measures 10 mm \times 8 mm with an etching depth of 20 μm , and the pore size distribution ranges from 20 to 240 μm , with an average of approximately 96.4 μm . The pore size frequency distributions of rock samples and microscopic models are shown in Fig. 2. During the construction of the microscopic model, some pores from the cast thin sections were connected and corrected,

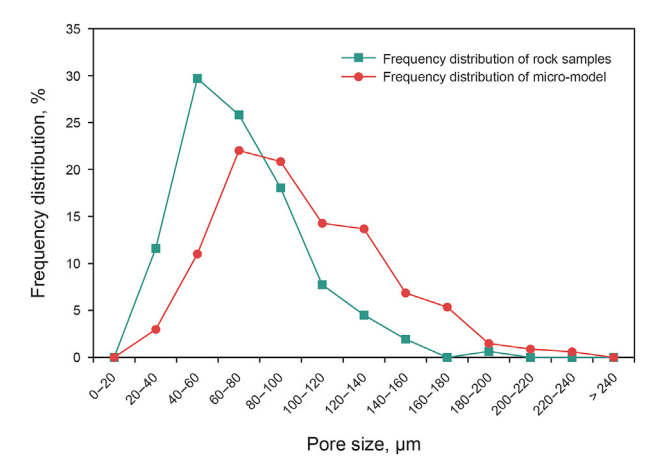


Fig. 2. Pore size frequency distribution of rock samples and the micromodel.

resulting in a higher porosity in the etched microscopic model compared to the cast thin sections. This adjustment aimed to enhance the overall connectivity of the pore network in the model, ensuring continuous fluid flow and operational feasibility while simplifying complex pore structures. This makes the model more suitable for studying fluid flow and diffusion at the microscopic level. Although the initial wettability of the etched microscopic model was water-wet, it is weaker compared to that within the rock. Therefore, to maintain similarity with the wettability behavior of the actual cast thin sections, the study appropriately enlarged the pore sizes to compensate for capillary pressure changes caused by smaller wettability angles. By injecting water into the model, the permeability was calculated to be approximately 26.33 mD using Darcy's law, based on the pressure differential and injection rate. Additionally, image recognition software was used to calculate the porosity of the micro-model (chip) to be 35%.

2.2. Experimental equipment and samples

The experimental crude oil sample used in this study was taken from the ground degassed oil of Block G in the Shengli Oilfield. The various properties of the crude oil under subsurface temperature and pressure conditions are listed in Table 2. The density of the degassed crude oil is 0.87 g/cm³. The oil composition data is shown in Fig. 3. The kerosene used for blending the crude oil was sourced

Table 2 Formation crude oil parameters.

| Viscosity, mPa·s | Density, g/cm ³ | Volume coefficient | Gas—oil ratio, m ³ /m ³ | Saturation pressure, MPa |
|------------------|----------------------------|--------------------|---|--------------------------|
| 2.46 | 0.79 | 1.144 | 37.6 | 10.18 |

from Shanghai Aladdin Biochemical Technology Co., Ltd., with a primary component of pentadecane ($C_{15}H_{32}$) and a room temperature density of 0.79 g/cm³. The CO₂ gas sample used was produced by Qingdao Xinkeyuan Gas Company and has a purity of 99.99%.

The micro-scale visualization experimental setup comprises four main components: a micro-model reservoir simulation system, an injection system, a production system, and a data acquisition system. An illustrative diagram of the setup is shown in Fig. 4. The equipment is engineered to withstand temperatures up to 100 °C and pressures up to 70 MPa. Key instruments include a highprecision microscope, a sample container, a chip loading platform, a Vindum pump, a vacuum pump, a backpressure pump, and a confining pressure pump, among others. The confining pressure pump features pressure tracking capabilities to prevent chip damage from excessive internal pressure. The gas boost pump is equipped with a unidirectional valve for rapidly pressurizing CO₂ gas to the desired level. The confining pressure pump applies pressure to the chip while simultaneously heating the liquid within the chip loading platform. The backpressure pump regulates the outlet pressure, maintaining an accurate pressure gradient between the injection and production ends. Positioned above the chip, the high-precision microscope is integrated with a camera system to capture real-time fluid flow within the chip.

2.3. Experimental procedure

The experimental study was carried out in the G block of Shengli Oilfield, China, where the initial reservoir pressure was 42.6 MPa. Due to recent development activities, the reservoir pressure has decreased to 20 MPa. The experimental temperature was maintained at 50 $^{\circ}$ C, exceeding the critical temperature of carbon dioxide, and the backpressure was set to the current reservoir pressure of 20 MPa, ensuring that the injected CO₂ remained in a supercritical state. The primary experimental procedures are as follows.

(1) The crude oil was filtered under pressure to remove impurities using a filter paper with a pore size of 1 μ m, at a temperature of 50 °C and a pressure of 10 MPa. After filtration, the filter paper was checked for integrity; if it was damaged, a second filtration was performed.

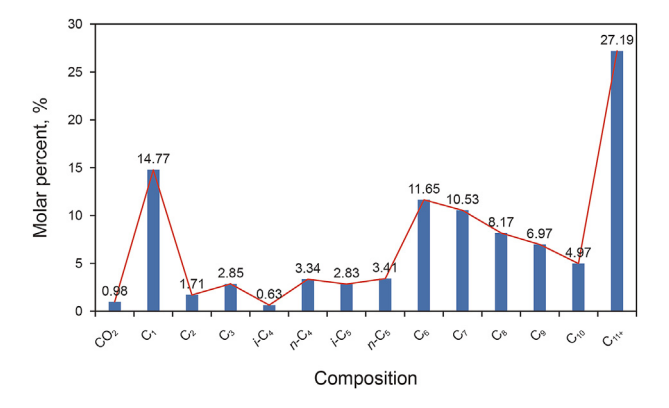


Fig. 3. Composition of the oil phase.

(2) The filtered crude oil was mixed with kerosene ($C_{15}H_{32}$) to measure its viscosity, which was then compared to the reservoir crude oil viscosity to ensure it fell within an acceptable error range. The viscosity of the blended oil sample was determined to be 2.53 mPa·s, with a relative error of 2.84%.

- (3) An organic solvent (petroleum ether) was used to clean the equipment pipelines and containers.
- (4) The Vindum pump was employed to inject the oil sample into the pore space of the chip, ensuring the space was completely filled with the blended oil.
- (5) The gas container was pressurized with CO_2 to 20 MPa using a gas booster pump in preparation for high-pressure gas injection.
- (6) The entrance valve of the chip was closed, and CO₂ gas injection commenced. The gas flow flushed the crude oil out of the pipelines. During this process, the gas booster pump continuously maintained the gas pressure in the gas sample container.
- (7) Before conducting the displacement experiment, the gas is initially advanced at one-tenth of the experimental displacement rate. Once the oil—gas front reaches the visible range, the displacement pump flow rate is adjusted to the experimental displacement rate to begin the experiment. This approach minimizes the impact of residual oil in the dead volume between the chip inlet and the exhaust valve on the experimental results.
- (8) CGI: CO₂ was continuously injected at a constant rate of 0.02 mL/min, with both the outlet and inlet valves of the chip open until no oil was produced at the outlet. The displacement speed used in this study was derived from the actual injection rate of the field injection well, based on Reynolds number similarity and geometric scaling. Specifically, the similarity criteria for scaling experimental models include geometric similarity, flow similarity, and dynamic similarity (Chanson, 2009). Dynamic similarity refers to mechanical similarity, which serves as the primary factor influencing flow similarity, while flow similarity is a manifestation of dynamic similarity (Durst, 2022). Therefore, under the assumption of dynamic similarity, flow similarity can be somewhat overlooked. Overall, the similarity criteria for underground reservoir seepage experiments primarily focus on dynamic and geometric similarity. Currently, there is no established similarity theory for parameter conversion in micro-experiments. Therefore, in consideration of the specific issues addressed in this study, geometric similarity primarily focuses on the similarity of seepage area. In actual field production, the seepage area is defined as the product of perforation length and wellbore circumference. In microexperiments, the seepage area is calculated as the product of the width and depth of the etched region on the chip. The seepage area in micro-experiments is significantly smaller than that in field conditions, making direct similarity ratios impractical. Therefore, this study focuses solely on the variation in seepage length, simplifying geometric similarity to the ratio of seepage lengths, as given by the following formula:

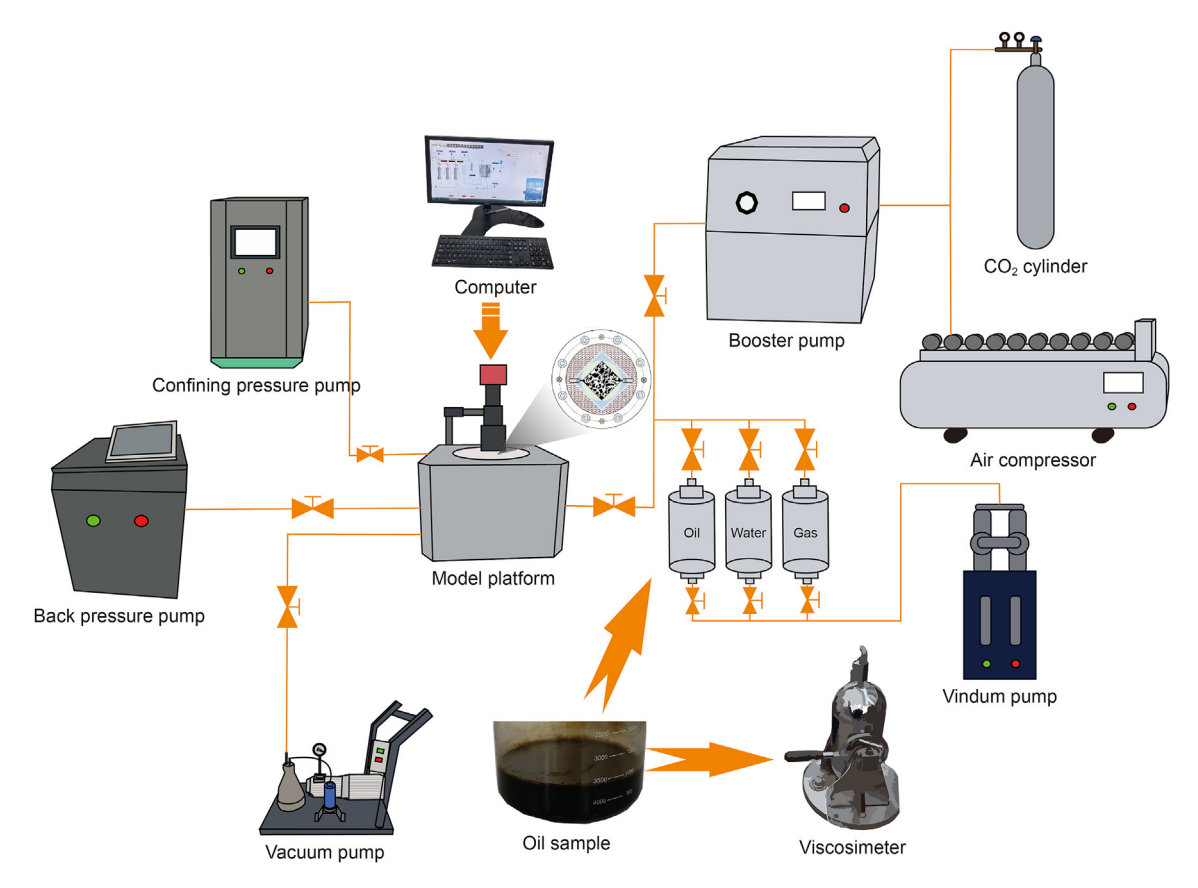


Fig. 4. Schematic diagram of experimental apparatus.

$$\alpha_1 = \frac{H_s}{H_e} \tag{1}$$

where α_1 is the geometric similarity coefficient; H_s is the field seepage length, m; H_e is the experimental seepage length, m.

There are currently three main criteria for dynamic similarity. First is the Reynolds criterion, which maintains equal Reynolds numbers to ensure viscous force similarity (Heller, 2017). The second is the Froude criterion, which requires equal Froude numbers to maintain gravitational similarity (Lin et al., 2021). The third is the Euler criterion, which maintains equal Euler numbers, corresponding to pressure similarity (Ryutov et al., 1999). In underground micro-seepage processes, viscous forces are dominant, so dynamic similarity typically employs the Reynolds number criterion. Therefore, this study adopts the Reynolds number criterion for dynamic similarity adjustments, with the following calculation formula:

$$\alpha_2 = \frac{V_s}{V_e} = \frac{\rho_s D_s \mu_e}{\rho_e D_e \mu_s} \tag{2}$$

where α_2 is the flow similarity coefficient; V_s is the field seepage velocity, m/s; V_e is the experimental seepage velocity, m/s; ρ_s is the field fluid density, kg/m³; ρ_e is the experimental fluid density, kg/m³; μ_s is the field fluid viscosity, mPa·s; μ_e is the experimental fluid viscosity, mPa·s; D_s is the field characteristic length, m; D_e is the experimental characteristic length, m.

Based on considerations of geometric and dynamic similarity, it is essential to ensure that microfluidic experiments reflect fluid behavior consistent with field conditions, maintaining similarity in fluid storage and flow characteristics. Therefore, when converting

injection rates between field and experimental conditions, it is necessary to account for differences in porosity. This study incorporates the porosity ratio of both conditions for the conversion. By combining Eqs. (1) and (2), the conversion formula for injection rates between field and experimental conditions is as follows:

$$\frac{Q_s}{Q_e} = \alpha_1 \alpha_2 \frac{\phi_s}{\phi_e} \tag{3}$$

where Q_s is the field injection rate, m^3/d ; Q_e is the experimental injection rate, m^3/d ; ϕ_s is the field porosity; ϕ_e is the experimental chip porosity.

The characteristic length is the representative length scale describing the geometric or physical features of the system. In this study, the experimental characteristic length is chosen as the length of the etched area of the chip (10 mm) for calculating the flow similarity coefficient. Since the study focuses on localized injection analysis, the field characteristic length is selected as the effective thickness of the reservoir (20.5 m). The fluid density and viscosity used in the experiment are similar to those in the field and are thus ignored in the calculations. Therefore, the flow similarity coefficient is calculated as 2050. For the seepage area scaling factor, the field seepage length is the effective thickness of the reservoir (20.5 m), and the experimental seepage length is the width of the chip (8 mm). Thus, the seepage area scaling factor is calculated as 2562.5. The average field porosity is 14%, and the chip porosity is 35%. The field gas injection rate is 65 m³/d, which, according to Eq. (1), is converted to an experimental injection rate of approximately 0.021 mL/min. In the experiment, an injection rate of approximately 0.02 mL/min was used.

- (9) AIP: Based on synchronized continuous gas injection, the outlet valve was closed, and CO₂ was injected at a rate of 0.02 mL/min for 30 min. The inlet valve was then closed, soaking for 30 min, followed by simultaneous opening of the outlet and inlet valves for constant-rate displacement for 30 min. High-speed asynchronous injection—production (HAIP): Building on asynchronous injection—production, the injection—production speed was increased to 0.05 mL/min, repeating the asynchronous injection—production experiment. In this context, the displacement time is set based on the duration of CGI, which is approximately 30 min. This approach is used to investigate the impact of altering injection and production methods on EOR and the distribution of residual oil.
- (10) SCI: Both the outlet and inlet valves were opened, injecting CO₂ at a rate of 0.02 mL/min for 30 min. Subsequently, both the inlet and outlet valves were closed, stopping injection and production for 30 min. This cycle was repeated four times, with the injection rate increased to 0.04 mL/min for the last two cycles.

3. Results and discussion

In order to analyze the displacement effect more effectively, this article categorizes the remaining oil into five states: corner-shaped, droplet-shaped, membrane-shaped, column-shaped, and porous-shaped (Su et al., 2022), as shown in Fig. 5. The characteristics of residual oil in different states are as follows: (1) Membrane: typically adheres to the inner walls of individual pore throats (Fig. 5(a)). (2) Column: found in the throats connecting pores (Fig. 5(b)). (3) Cluster: residual oil distributed in small pores, often continuous across three or more pores (Fig. 5(c)). (4) Droplet: multiple small, discrete oil droplets within a single pore. These droplets are relatively uniform in shape and are often found in larger pores (Fig. 5(d)). (5) Corner: usually located in the corners or blind ends of complex pore spaces, with one side attached to the pore wall and the other side in the throat space of the pore (Fig. 5(e)).

In this section of the study, quantitative characterization was conducted for the microscopic oil recovery rate, residual oil saturation, and dynamic expansion coefficient of crude oil. The calculation formulas for each parameter are as follows.

(1) Microscopic oil recovery

$$\eta = \frac{S_{\text{reo}}}{S_0} \tag{4}$$

where η represents the microscopic oil recovery rate, %; S_{reo} is the area of remaining oil distribution under gas drive, μm^2 ; S_0 is the total area of saturated oil, μm^2 .

(2) Remaining oil ratio

$$\lambda = \frac{S_1}{S_0} \tag{5}$$

where λ denotes the remaining oil ratio, %; S_1 is the area of remaining oil at the same saturation state, μm^2 ; S_0 is the total area of saturated oil, μm^2 .

(3) Dynamic expansion coefficient of oil

$$\zeta = \frac{V_{\rm c}}{V_{\rm c}} \tag{6}$$

where ζ represents the dynamic expansion coefficient of oil; V_c is the volume change of oil, μm^3 ; V_o is the original volume of oil, μm^3 .

3.1. Analysis of characteristics of CGI

The mechanism of CO₂ flooding is generally studied in three aspects: non-miscible displacement, near-miscible displacement, and miscible displacement. The typical boundary to distinguish the displacement characteristics mentioned above is the minimum miscible pressure between CO₂ and crude oil. The results of fitting the crude oil PVT experimental data and related parameters using the CMG WinProp module are shown in Fig. 6. The software estimates that the pressure at which the crude oil sample used in this study becomes miscible with CO₂ is 19.2 MPa.

In the initial stage of simultaneous injection and production, the CO₂ gas front comes into contact with the crude oil, forming a transition zone. Within this zone, CO₂ dissolves and extracts components from the crude oil, causing the oil to lighten in color while dark, heavy components are removed (as shown in Fig. 7). When the crude oil has not yet reached CO₂ saturation, the primary interaction between the oil and CO₂ is dissolution, leading to a color change in the crude oil without the appearance of free CO₂, which

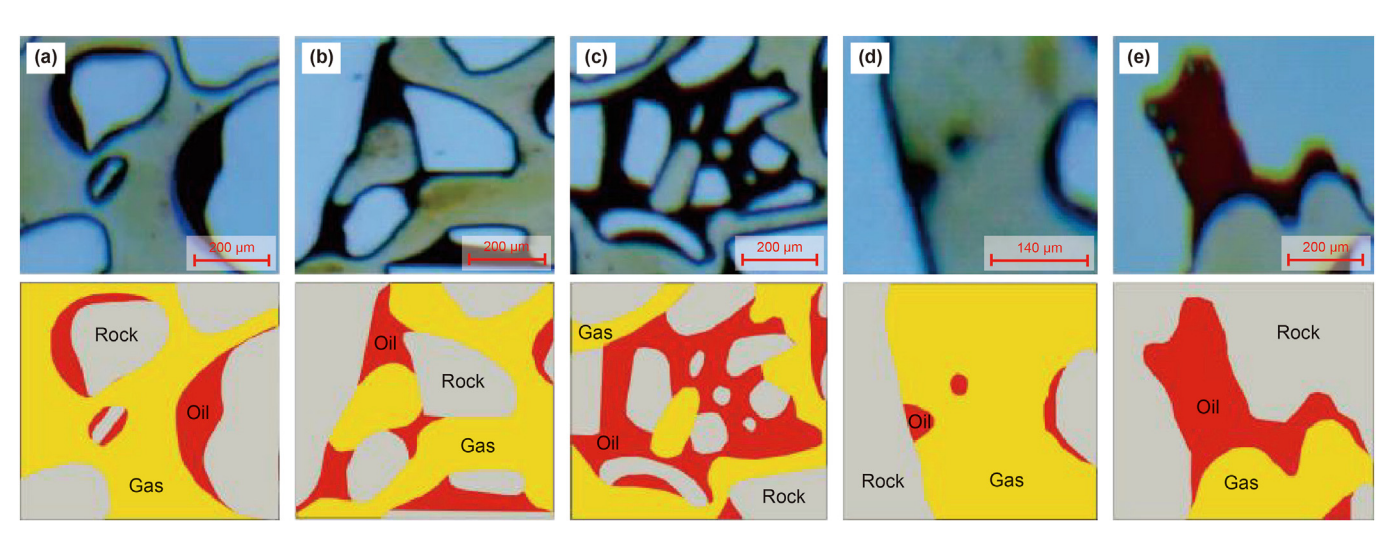


Fig. 5. The residual oil distribution state: (a) membrane oil, (b) column oil, (c) cluster oil, (d) droplet oil, (e) corner oil.

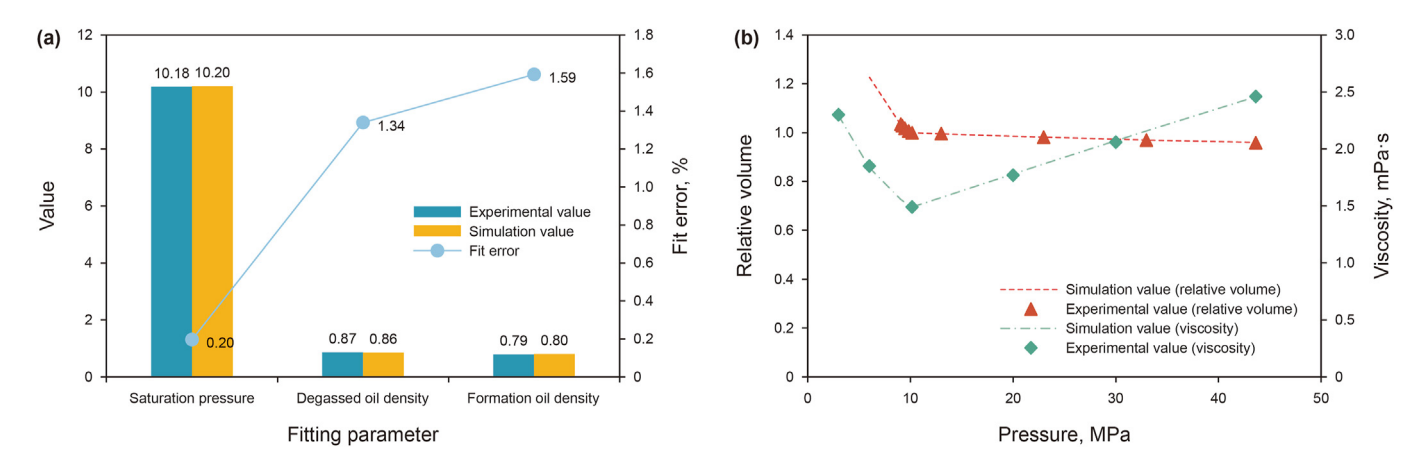


Fig. 6. Fitting results of the numerical simulation model with PVT experimental data and related parameters: (a) fitting results of saturation pressure and density, (b) fitting results of relative volume and viscosity under different pressures.

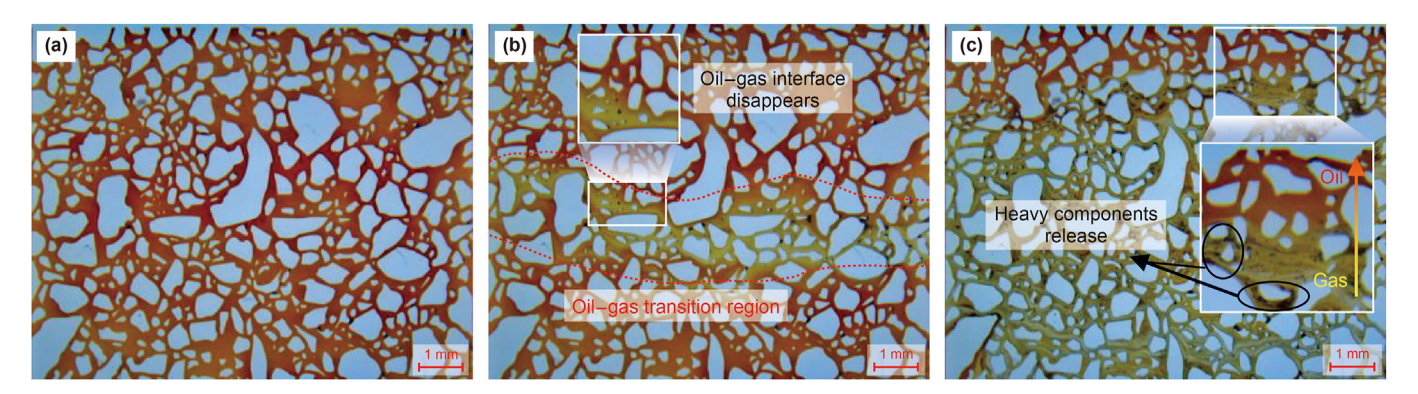


Fig. 7. Distribution of residual oil at each time of CGI: (a) initial state (0 s), (b) mixed phase (1 s), (c) asphaltene release (11 s).

typically occurs at the leading edge of CO₂ flooding. During continuous gas injection, the migration pattern of the oil—gas front and CO₂ generally follows the "near, low resistance" principle, meaning the transition zone moves in a straight line path between injection and production wells. In the diffusion process of the oil—gas transition zone, the interface between the crude oil and gas becomes blurred, lacking a distinct boundary. Based on the minimum miscibility pressure (MMP) results, it can be inferred that CO₂ initially displaces crude oil in a near-miscible manner.

As displacement progresses into the later stages of CGI, the oil sample's color darkens. This occurs because, when CO₂ in the crude oil reaches saturation, free CO₂ contacts the oil and extracts lighter components, leading to a darker appearance (reduced gray value). Concurrently, CO₂ enrichment primarily takes place at the oil—gas interface. Closer to the injection point, the extraction effect of CO₂ intensifies (Ding et al., 2017), further reducing the crude oil's gray value (as shown in Fig. 8). In these later stages, the CO₂ extraction alters the crude oil composition, increasing the minimum miscible pressure with CO₂. Consequently, the oil—gas interface becomes more distinct. Therefore, non-miscible displacement predominates in the later stages of CO₂ injection.

3.2. Analysis of CO₂-EOR mechanism in AIP

For AIP, pre-injection of CO₂ resulted in a pressure increase of 0.96 MPa within the chip. For HAIP, pre-injection of CO₂ caused a pressure increase of 1.69 MPa in the chip. Therefore, based on the gas state equation, the volume of CO₂ injected during the pre-injection phase for AIP is calculated to be 0.05 pore volumes (PV).

For HAIP, the volume of CO₂ injected during the pre-injection phase is calculated to be 0.085 PV. To quantitatively analyze the remaining oil under various injection and production methods, this study performed a statistical analysis of microscopic oil recovery, as illustrated in Fig. 9. Compared to synchronous continuous gas flooding, asynchronous injection and production methods achieved a 6.58% increase in oil recovery in the observed area. This improvement is primarily due to the fact that during the injection and shut-in phases of asynchronous methods, the internal pressure within the micro-model rises, facilitating thorough contact and dissolution expansion of CO₂ with the crude oil. This dissolution expansion effect enhances the elasticity of the oil system, thereby improving the overall oil recovery process. Both AIP and HAIP methods demonstrated similar final oil recovery rates, suggesting that increasing the displacement rate in asynchronous injection and production has a limited additional impact.

In contrast, during simultaneous continuous gas flooding, gas flow is concentrated in a dominant channel, limiting its impact on the remaining oil outside this main channel. In the injection and production coupling process, significant pressure field variations allow for the mobilization of more residual oil. For example, in the case of clustered residual oil at positions A and B after soaking (Fig. 10), a radial pressure gradient forms around the injection point when only injection is performed. The fluid flow directions at points A and B are depicted as $V_{\rm In}$ in Fig. 10(b). When production begins and pressure increases, another radial pressure gradient forms around the extraction point, with the flow directions at points A and B shown as $V_{\rm Pro}$ in Fig. 10(b). Compared to the flow direction $V_{\rm C}$ in simultaneous continuous gas flooding, the flow

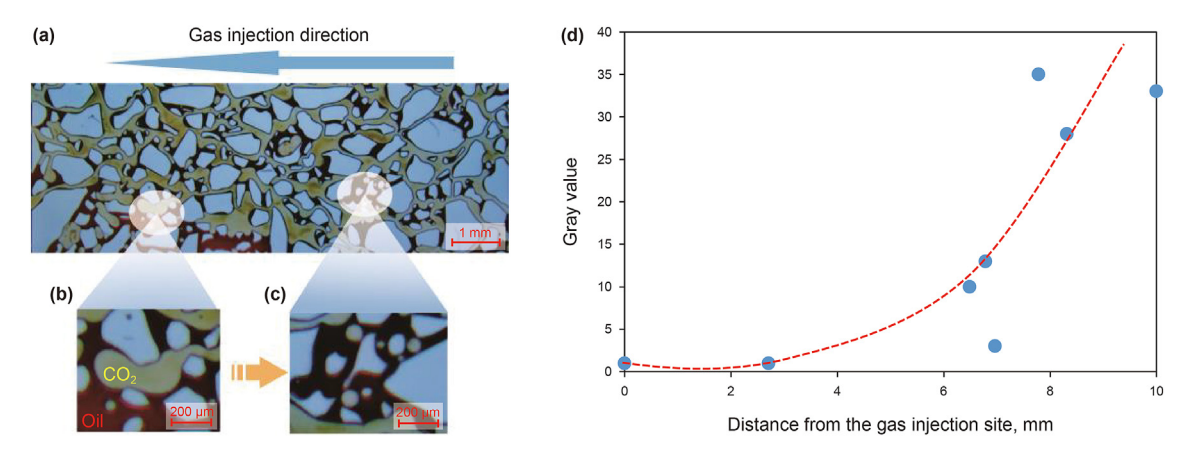


Fig. 8. The CO₂ extraction effect: (a) distribution of remaining oil at 616 s after gas injection, (b) remaining oil status at the front end of gas injection, (c) remaining oil status at the rear end of gas injection, (d) variation of crude oil color gray values at different distances from the gas injection point.

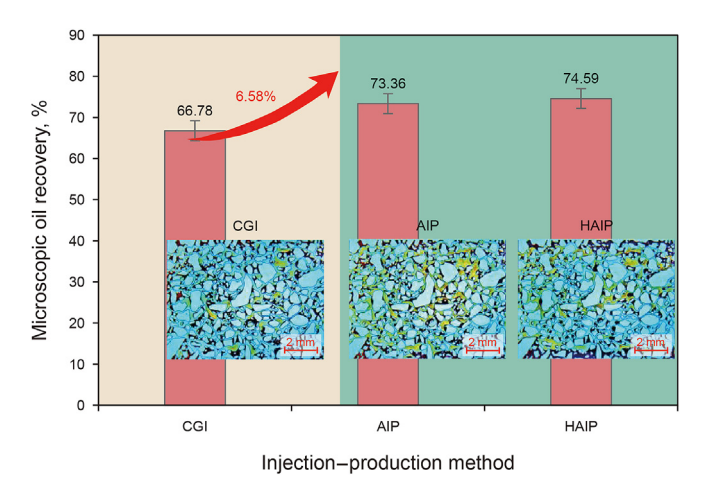


Fig. 9. Microscopic oil recovery under different injection and production methods.

direction in injection and production coupling changes markedly, which broadens the coverage of the injected gas and enhances oil recovery.

Fig. 11 illustrates the distribution of remaining oil for CGI and AIP coupling. After simultaneous injection and production, the remaining oil primarily consists of clustered residual oil located in less favorable regions. Upon applying the respective injection and production coupling methods, the clustered residual oil is displaced, resulting in the formation of more easily transportable membrane and columnar residual oil. Consequently, the amount of clustered residual oil decreases significantly in AIP, while the quantities of membrane and columnar residual oil increase.

Before analyzing the mobilization mechanisms of different remaining oil, it is necessary to understand their mechanical action. Here, we select the membrane oil for force analysis. It can be observed that the airflow on both sides of the membrane-shaped oil exerts shear forces $F_{\rm s1}$ and $F_{\rm s2}$ on the oil droplets, respectively. When the combined force $F_{\rm s}$ is equal to the adhesion force $F_{\rm v}$ between the oil droplets and the solid surface, this portion of residual oil exists in the form of membrane-shaped oil. Fig. 12 illustrates the force acting on the oil droplets by the airflow. In other words

$$F_{\rm S} + F_{\rm V} = 0 \tag{7}$$

where F_S is the shear traction force of the airflow, N; F_V is the adhesion force between the oil droplets and the solid surface, N; F_S

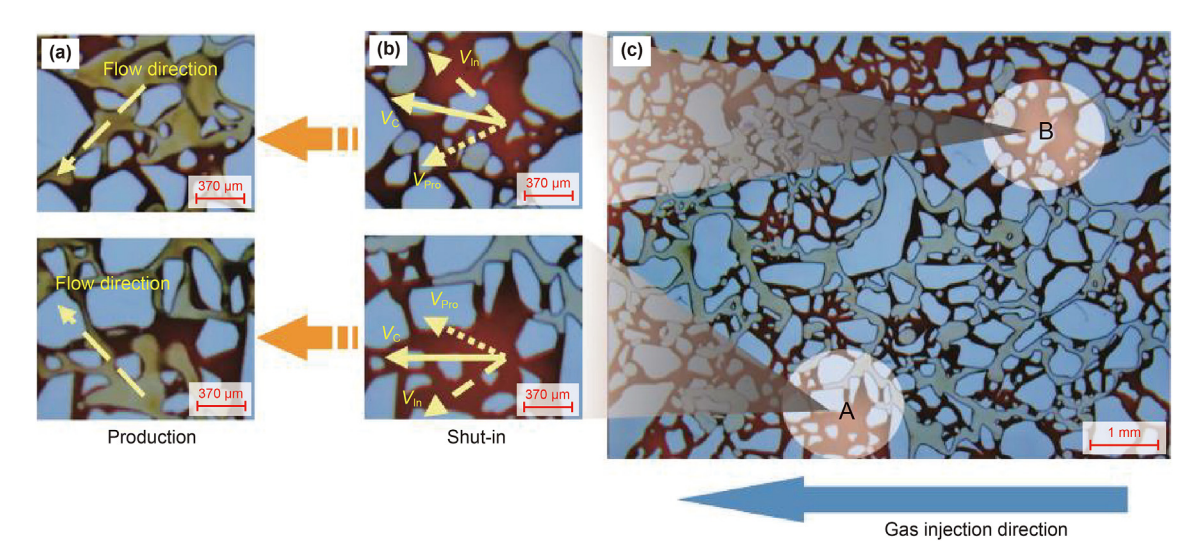


Fig. 10. Direction of injection—production coupled fluid flow: (a) remaining oil flow directions during production stages A and B, (b) remaining oil saturation status and schematic of injection and production flow directions during shut-in stages A and B, (c) distribution of remaining oil during the AIP shut-in stage.

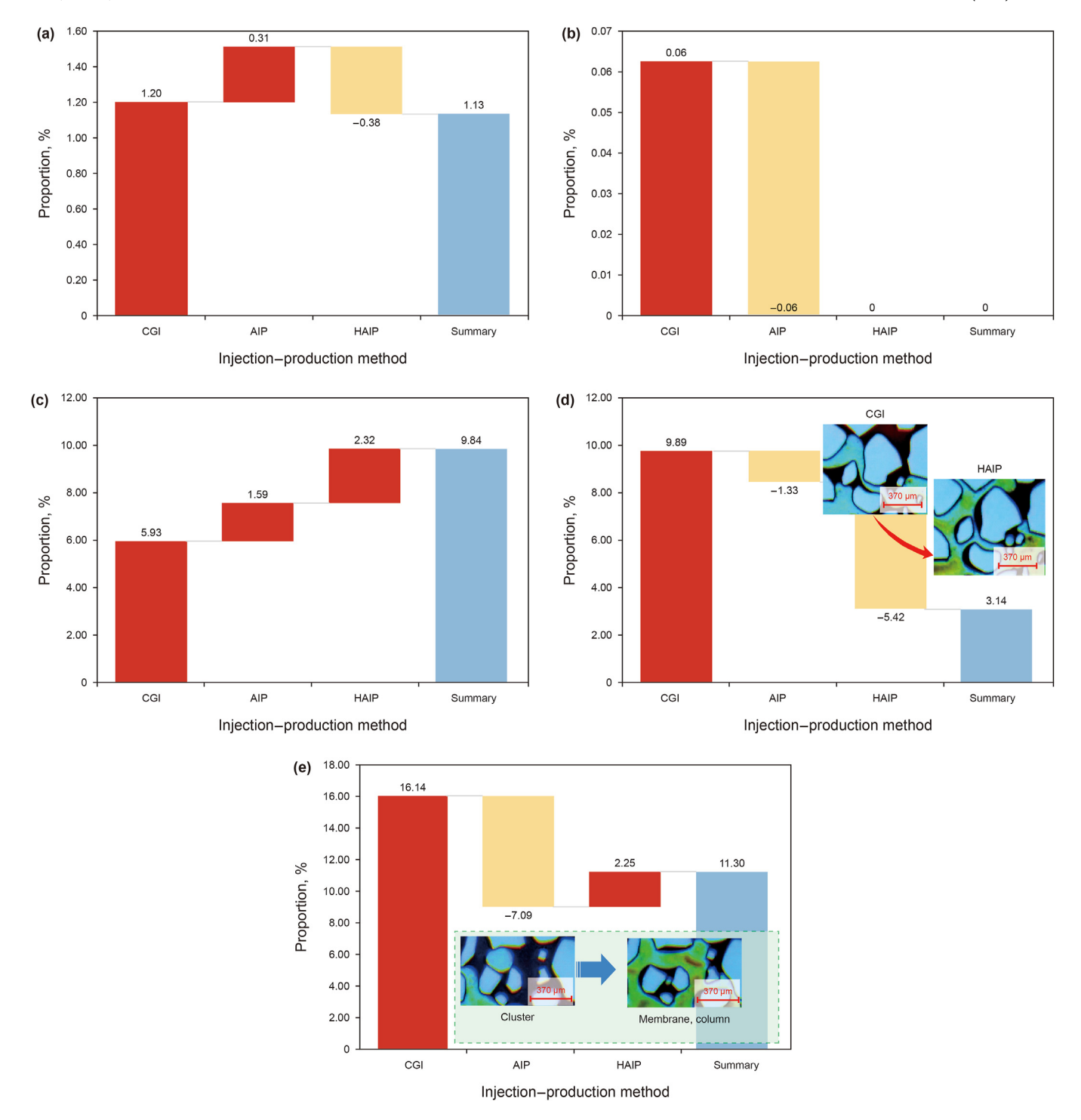


Fig. 11. Proportion of residual oil distribution in different injection and production methods: (a) corner oil, (b) droplet oil, (c) membrane oil, (d) column oil, and (e) cluster oil.

is the sum of F_{s1} and F_{s2} .

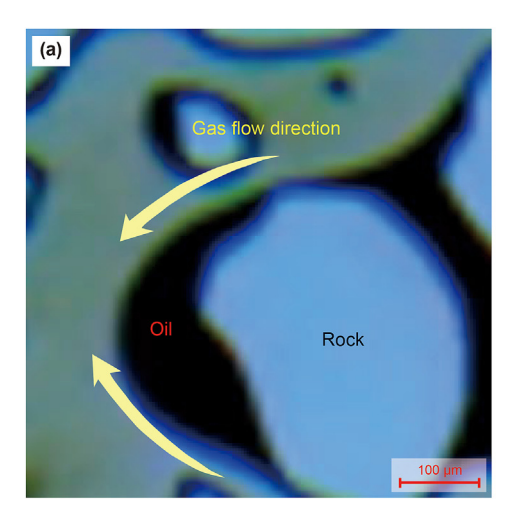
Sugiyama and Sbragaglia (2008) provided expressions for various forces acting on a semi-spherical liquid droplet in three-dimensional shear flow in early research. The formula for the traction force generated by the shear action of the airflow is as follows:

$$F = k_{x^2} (4.3\pi R \cdot \mu \cdot V_{\text{air}}) \tag{8}$$

where k_{x^2} is the wall correction coefficient; R is the radius of the oil

droplet, mm; $V_{\rm air}$ is the airflow velocity, mm/s; μ is the gas viscosity, mPa·s.

Due to the irregularity of the solid surface in this model, the oil droplets are not perfect semi-spheres. Therefore, the radius of the oil droplet in the formula can be replaced by the effective radius. The calculation formula for the effective radius of the oil droplet is shown in Eq. (9). Additionally, using the relationship of shear stress in Eq. (10), the traction force generated by the airflow can be expressed in terms of shear stress. The final calculation formula for the airflow shear traction force is shown in Eq. (11).



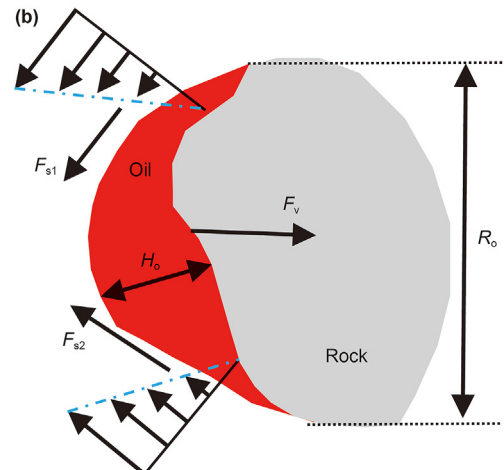


Fig. 12. Occurrence state of membrane oil (a) and schematic of force analysis on membrane oil (b).

$$R_{\rm ef} = \sqrt{H_0 \times \frac{R_0}{2}} \tag{9}$$

where $R_{\rm ef}$ is the effective radius of the oil droplet, mm; $H_{\rm o}$ is the height of the oil droplet on the solid surface, mm; $R_{\rm o}$ is the diameter of the circle tangent to the fluid—solid interface, mm.

$$\tau = \frac{\mu \times V_{\text{air}}}{R} \tag{10}$$

where τ represents shear stress, Pa.

$$F_D = k_{\chi^2} \left(4.3 \pi R_{\text{ef}}^2 \cdot \tau \right) \tag{11}$$

On the other hand, another factor contributing to the stable retention of oil droplets is the adhesion force generated by the contact between the oil droplet and the solid surface. This force represents the resistance of the residual oil droplet to detach from the matrix wall. Assuming the oil droplet maintains an elliptical contact line during retention, this force can be expressed as

$$F_{V} = -\sigma R_{0} \int_{0}^{\pi} \cos \theta(\alpha) \cos \alpha d\alpha$$
 (12)

where σ is the surface tension of the liquid, N/mm; $\theta(\alpha)$ is the contact angle between the oil droplet and the solid surface when the contact line forms an angle α , \circ , as shown in Fig. 13.

There are various methods to represent the contact angle between the oil droplet and the solid surface. Under the research conditions of this paper, the simplest approach is to assume a continuous relationship between the contact angles of the upper and lower sides of the oil droplet, with the contact angle variation exhibiting a linear relationship. Therefore, the change in the contact angle can be expressed by Eq. (13).

$$\theta = \begin{cases} \theta_{u} + \frac{2(\theta_{c} - \theta_{u})}{\pi} \alpha & 0 \leq \alpha < \frac{\pi}{2} \\ \theta_{c} - \frac{2(\theta_{c} - \theta_{b})}{\pi} \alpha & \frac{\pi}{2} \leq \alpha < \pi \end{cases}$$
(13)

where θ_u is the contact angle at the upper part, °; θ_c is the maximum contact angle at the center, assumed to be at 90° radians, °; θ_d is the contact angle at the lower part, °.

Substituting Eq. (13) into Eq. (12), we can derive the relationship

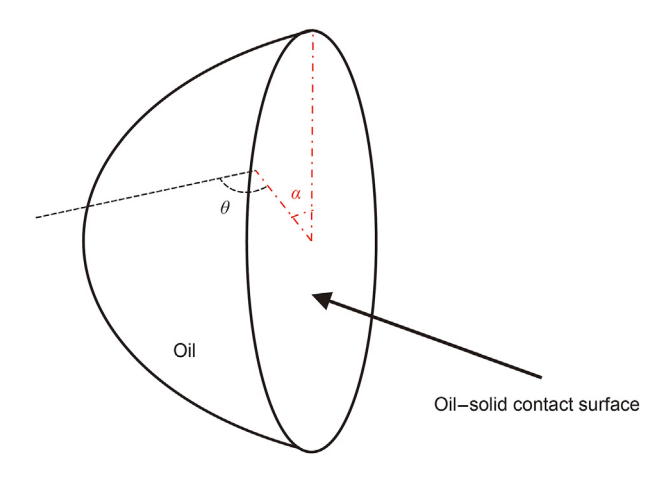


Fig. 13. The contact angle between the oil droplet and the solid surface (varying with α).

formula for the adhesion force between the oil droplet and the solid surface as shown in Eq. (14).

$$\begin{split} F_{v} &= -\sigma R_{o} \int_{0}^{\frac{\pi}{2}} \cos \left(-\theta_{u} - \frac{2(\theta_{c} - \theta_{u})}{\pi} \alpha \right) \cos \alpha d\alpha \\ &- \sigma R_{o} \int_{\frac{\pi}{2}}^{\pi} \cos \left(-\theta_{c} + \frac{2(\theta_{c} - \theta_{b})}{\pi} \alpha \right) \cos \alpha d\alpha \end{split} \tag{14}$$

Eq. (15) can be obtained by integration. According to the relationship, it can be seen that the sizes of the contact angles at the upper and lower sides of the oil droplet are closely related to the effective radius of the oil droplet. When the contact angles on both sides change under the action of airflow shear force, the volume of the retained oil droplet will also change, resulting in airflow erosion.

$$F_{v} = -\frac{2\sigma R_{o}}{\pi} \left(\frac{\sin(\theta_{c} - \theta_{u})}{2} + \frac{\pi \cos(\theta_{c} - \theta_{u})}{4} \right) - \sigma R_{o} \left(-\frac{2}{\pi} \left(\frac{\sin(\theta_{b} - \theta_{c})}{2} + \frac{\pi \cos(\theta_{b} - \theta_{c})}{4} \right) \right)$$

$$(15)$$

During the injection and soaking stages, the membrane oil undergoes movement under the action of adhesion force F_v , transforming into a more stable column-shaped oil. Therefore, after the

soaking stage, the predominant retention states of the residual oil are porous and column-shaped (as shown in Fig. 14(a)), facilitating subsequent exploitation. When production wells are opened, due to the increased pressure at the injection end, the driving force F_p generated by the pressure differential exceeds the adhesion resistance between the oil and the solid contact surface. Consequently, the crude oil moves in the direction of pressure drop, achieving exploitation (as depicted in Fig. 14(b)). The expression for F_p is given by Eq. (16).

$$F_{\rm p} = \Delta P \times \pi r_{\rm o} h_{\rm o} \tag{16}$$

where F_p is the driving force generated by the pressure difference, N; ΔP is the pressure difference between the two ends, Pa; r_0 is the width of the column oil, mm; h_0 is the thickness of the oil, mm.

Columnar oil typically resides in pore throats that are perpendicular to the displacement direction. The driving force (F_p) exerted by the pressure difference between the gas flow at the top and bottom of this columnar oil is relatively small compared to the adhesion force (P_v) at the oil—solid interface (Fig. 15(a)). As a result, this residual oil is challenging to be extracted. During the injection and soaking process, this residual oil generally remains stationary. However, surrounding membrane-shaped residual oil tends to aggregate with the columnar oil, forming a continuous oil phase (Fig. 15(b)). When production wells are opened, significant changes in the internal pressure field increase the gas driving force beyond its flow resistance (P_v) , facilitating the extraction of crude oil (Fig. 15(c)). Regarding the extraction mechanism of porous residual oil, it involves both dissolution and gas drive mechanisms, as illustrated in Fig. 16. During production, changes in the pressure field increase the pressure difference (ΔP) across the porous residual oil, allowing gas to displace the crude oil. Notably, CO₂ extraction can cause heavy components to deposit (Fig. 16(c)), which may block smaller pore throat channels and hinder the extraction of some residual oil.

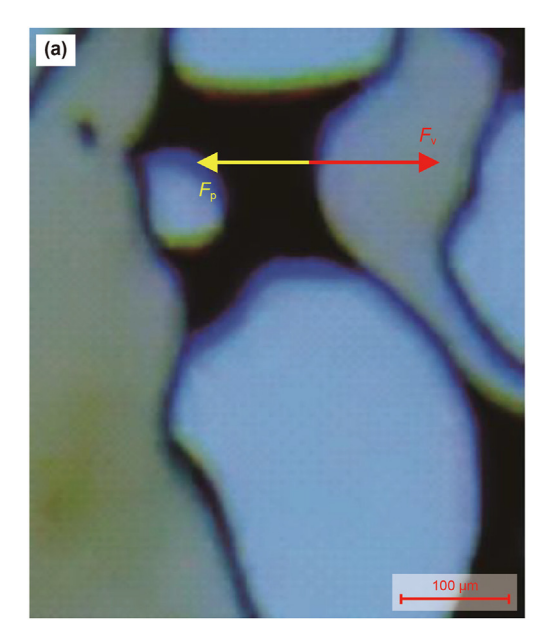
Overall, the experimental results reveal that in asynchronous injection—production methods, dynamic control of injection and production activities can significantly impact the microscopic oil recovery effects of CO₂. Specifically, in injection—production

coupling technology, precise control of the timing of injection and production allows for dynamic adjustment of the pressure field in the reservoir. This control enables CO_2 to dissolve fully in the crude oil during the injection phase, increasing the elasticity of the oil system and providing a stronger driving force. This effect has been shown to improve recovery rates in asynchronous injection—production experiments. During the injection—production coupling process, membrane and columnar oils redistribute under pressure changes and convert into more stable columnar or porous oils after the shut-in period. This redistribution of residual oil creates conditions for further recovery, allowing CO_2 to cover a larger area and mobilize more residual oil, thus further increasing crude oil recovery rates.

3.3. Analysis of CO₂-EOR mechanism in SCI

Periodic injection and production, which involves the periodic alternation of injection and production processes, is a production system that coordinates the operation of periodic gas injection and oil production. It is considered a coupling production method. Recent research indicates that periodic injection and production show significant potential for utilizing CO₂ gas (Shchipanov et al., 2022). This section will analyze the mechanisms of CO₂ utilization in the context of fully synchronized periodic injection and production.

Fully synchronous coupled periodic gas injection involves the simultaneous operation and cessation of both injection and production at the injection and production ends, cycling through multiple rounds. Fig. 17 illustrates the microscopic oil recovery degree and recovery rate across different rounds of injection—production modes. The oil recovery rate increases with the number of rounds, with the most significant increases occurring in the second and third rounds, where microscopic oil recovery rates rose by 3.64% and 10.05%, respectively. Compared to CGI, after four rounds of periodic gas injection, the microscopic recovery rate improved by 13.77%, and compared to AIP, the rate increased by 7.19%. Fig. 18 shows the distribution of residual oil across different rounds. In the second round, the recovery rate improves mainly through the utilization of membrane oil, with a 2.69% decrease in



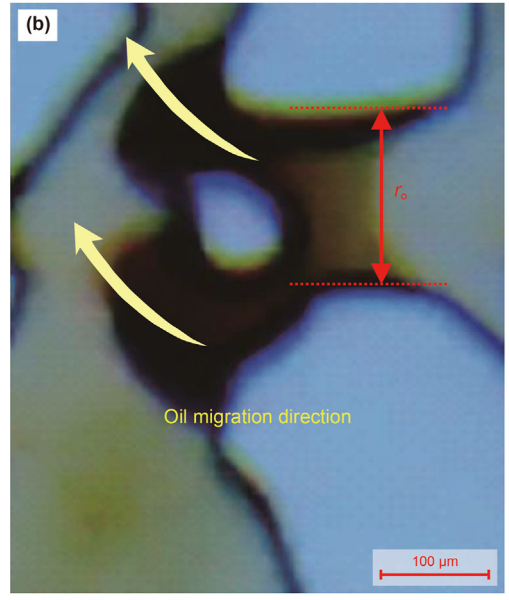


Fig. 14. Retention state of membrane-shaped oil during soaking and production stages: (a) transformation of membrane oil into column oil during soaking process and schematic of forces involved, (b) direction of crude oil exploitation during production stage.

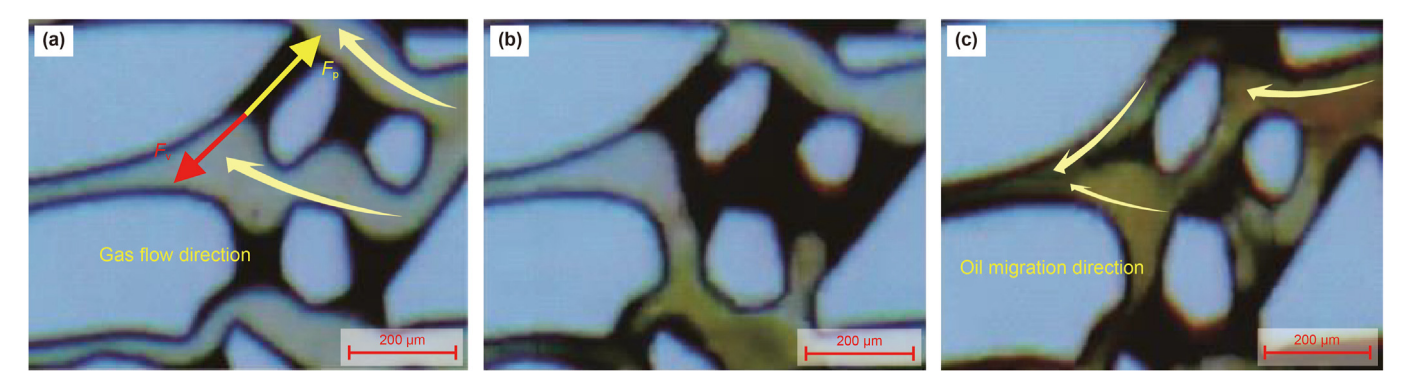


Fig. 15. The mobilization process of columnar residual oil: (a) the state of existence of columnar residual oil, (b) the increase in volume of columnar residual oil during the soaking stage, (c) the passive displacement of residual oil during the production stage.

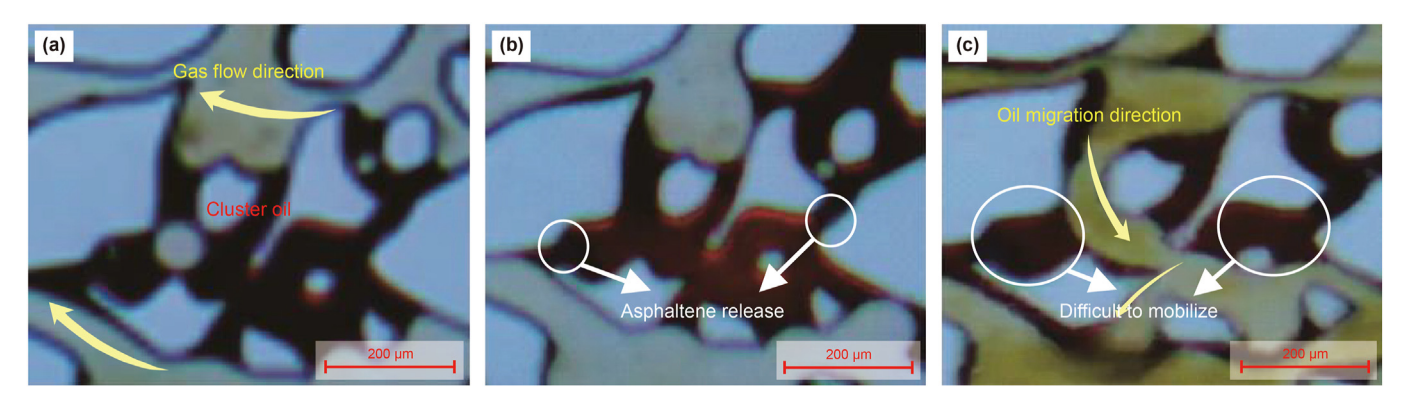
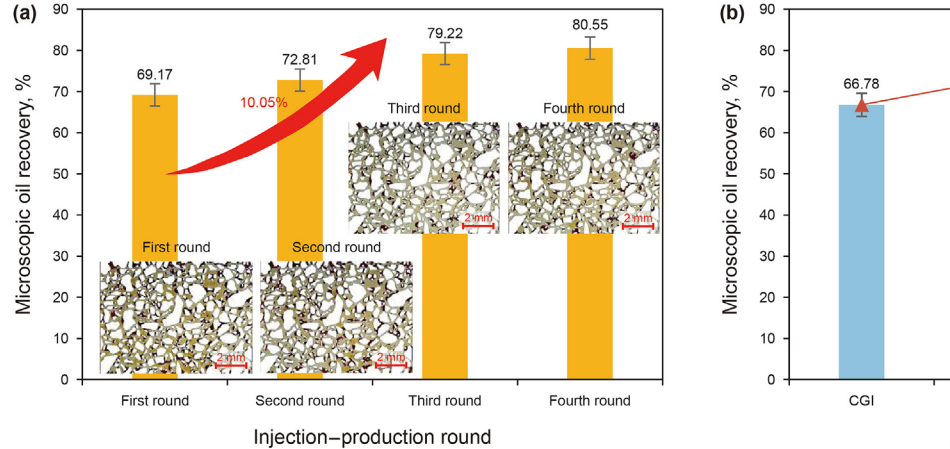


Fig. 16. The mobilization process of porous residual oil: (a) the state of existence of porous residual oil, (b) deposition of heavy components due to CO_2 extraction during the soaking stage, (c) a portion of the residual oil becomes difficult to mobilize due to the blockage caused by heavy components.

the proportion of membrane oil. In the third and fourth rounds, the conversion of porous residual oil into membrane and columnar oil leads to a 7.15% reduction in the proportion of porous residual oil. Fig. 19 compares the residual oil distribution under different injection—production modes. Both AIP and SCI modes show a significantly lower proportion of porous residual oil compared to CGI, decreasing by 7.1% and 12.8%, respectively. HAIP exhibits a more pronounced utilization of columnar residual oil, with its proportion decreasing by 6.8%. There is no significant change in the

final proportion of membrane oil under the injection—production coupling mode. This suggests that CGI, with its single gas channel, has relatively lower sweep efficiency and involves contiguous porous residual oil distribution. The injection—production coupling mode significantly reduces the proportion of this residual oil. However, due to pore adsorption forces, some residual oil remains as membrane and columnar oil during transportation. Thus, the injection—production coupling mode enhances microscopic oil recovery mainly through the effective utilization of porous residual



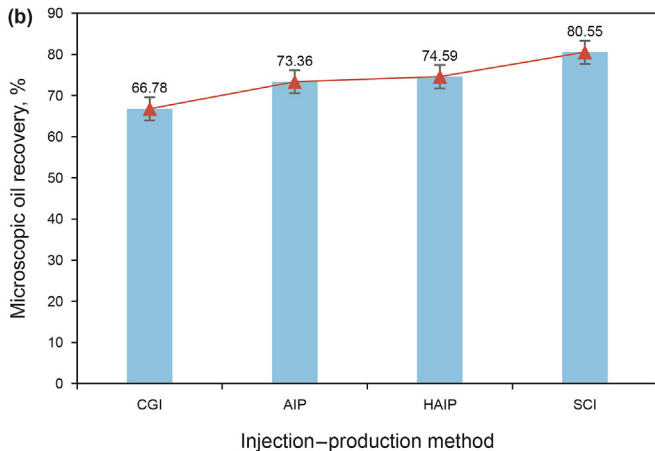


Fig. 17. Periodic gas injection CO₂-EOR effectiveness: (a) microscopic oil recovery at different cycles, (b) comparison of microscopic oil recovery rates under different injection—production modes.

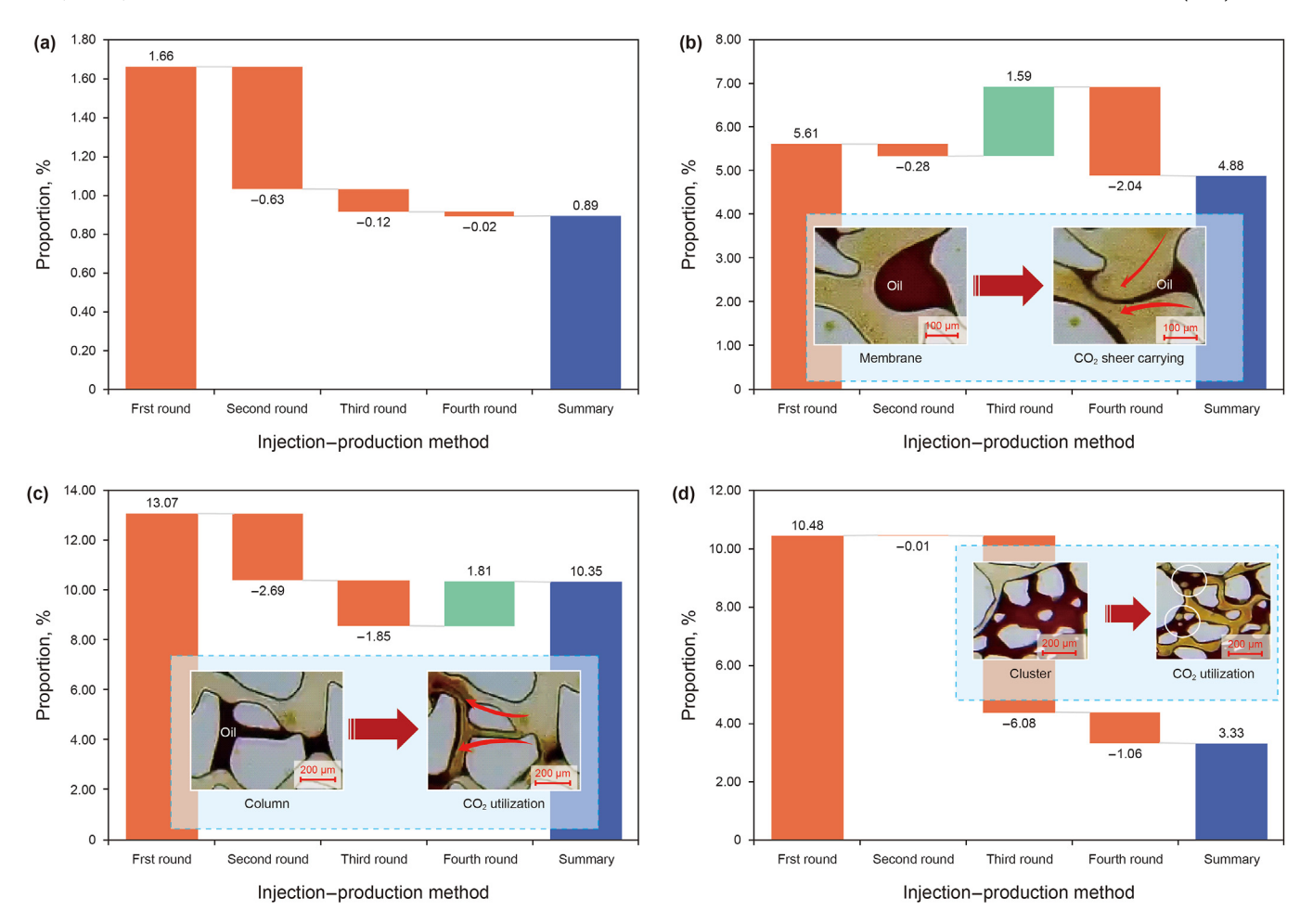


Fig. 18. Proportions of residual oil in different cycles: (a) corner oil, (b) membrane oil, (c) column oil, (d) cluster oil.

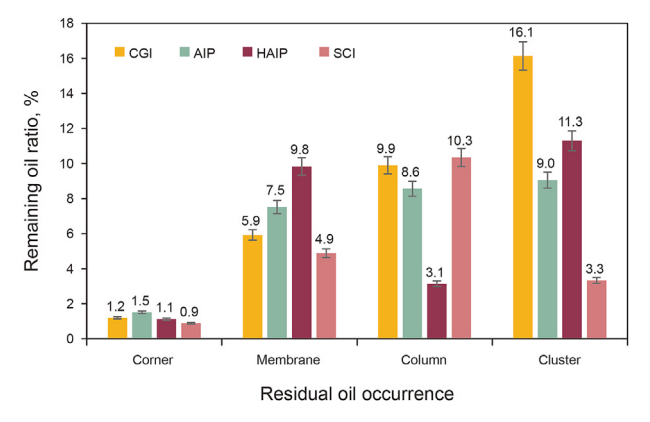


Fig. 19. Comparison of residual oil distribution under different injection—production modes.

oil.

During the stoppage phase of fully synchronized periodic injection and production, the absence of gas injection means that no additional energy is applied. Consequently, in the early stages of well production, the primary driving force for oil extraction is the elastic properties of the fluids themselves. Compared to CGI, the most notable improvement occurs during the stoppage and soaking phases after switching to periodic injection and production. During these phases, CO₂ dissolves into the oil, causing it to expand in

volume and thereby enhancing the elastic properties of the fluids within the model. When production resumes, the increased elastic energy can help mobilize some of the residual oil. Thus, from an energy perspective, the improved oil recovery with periodic injection and production compared to CGI is attributed to the higher overall energy available during periodic injection and production. The dynamic expansion coefficients of different residual oils during the shut-in soaking phase were calculated to analyze the volume expansion patterns of crude oil due to CO₂ dissolution, as shown in Fig. 20. The results indicate that as the residual oil in the pore throats undergoes dissolution expansion, the expansion coefficient increases linearly. However, once the crude oil expands to the throat opening, the force generated by the volume expansion is insufficient to overcome the capillary resistance. Consequently, the dynamic expansion coefficient of the crude oil labeled as 10 remains constant. Despite this, the reduced resistance facilitates the subsequent recovery of this portion of residual oil.

With the effect of elastic energy and subsequent gas injection for energy supplementation, the membrane-like oil experiences shear forces from the CO₂ gas flow on both sides, resulting in a filamentous flow pattern. An interesting phenomenon was observed during this process: when oil detaches under the influence of gas flow shear, vortices form on both sides as the gas flow interacts with the matrix solid. When the gas flow velocity is relatively high, the depressions on either side of the matrix solid start to influence each other. Fig. 21 illustrates the vertical movement trajectory of the oil phase. Since symmetry is never perfect at

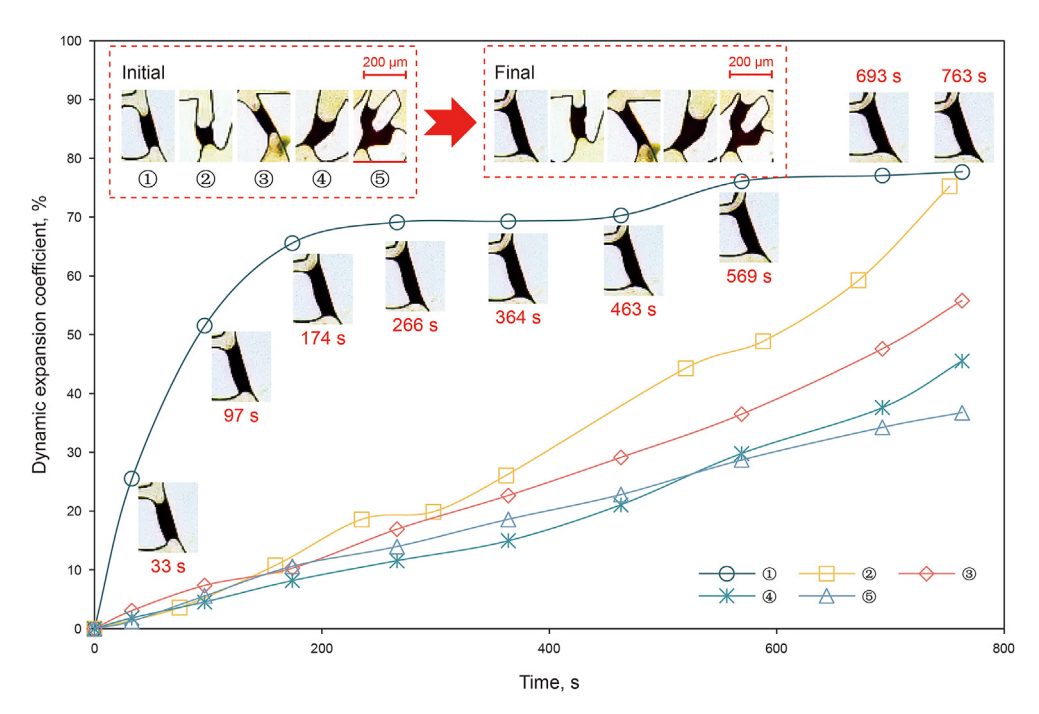


Fig. 20. The variation pattern of dynamic expansion coefficients for residual oil of different shapes and positions of occurrence.

any point, there is always one side with higher pressure and the other with lower pressure throughout the detachment of the membrane-like oil. This results in a reciprocating flow state, with the residual oil swinging up and down, confirming the presence of the Kármán vortex street phenomenon in porous media. Additionally, columnar residual oil can be mobilized by the CO₂ gas flow, which reduces the proportion of columnar residual oil. During the third and fourth cycles of injection and production, the release of energy disperses continuous porous oil into membrane-like and columnar oil. Concurrently, gas bubbles are released from the crude oil, enhancing the dissolution gas drive effect.

Another mechanism for exploiting residual oil through fully synchronized periodic gas injection involves the

expansion—migration process of residual oil. After completing one production cycle, some immobile membrane-like oil adhering to the wall (Fig. 22(a)) undergoes expansion due to the action of CO₂, transforming into columnar oil. Simultaneously, other membrane-like oils aggregate on the wall under capillary and elastic forces, increasing the volume of the original columnar oil (Fig. 22(b)), which facilitates its flow. During well production, CO₂ gas flow can then propel this portion of the original oil into adjacent areas, achieving residual oil extraction (Fig. 22(d)). In the production and exploitation phase, the force analysis of this portion of original oil is illustrated in Fig. 23. The driving force during well production equals the pressure difference multiplied by the vertical projection area of the contact surface (Eq. (17)). However, during CO₂ gas flow,

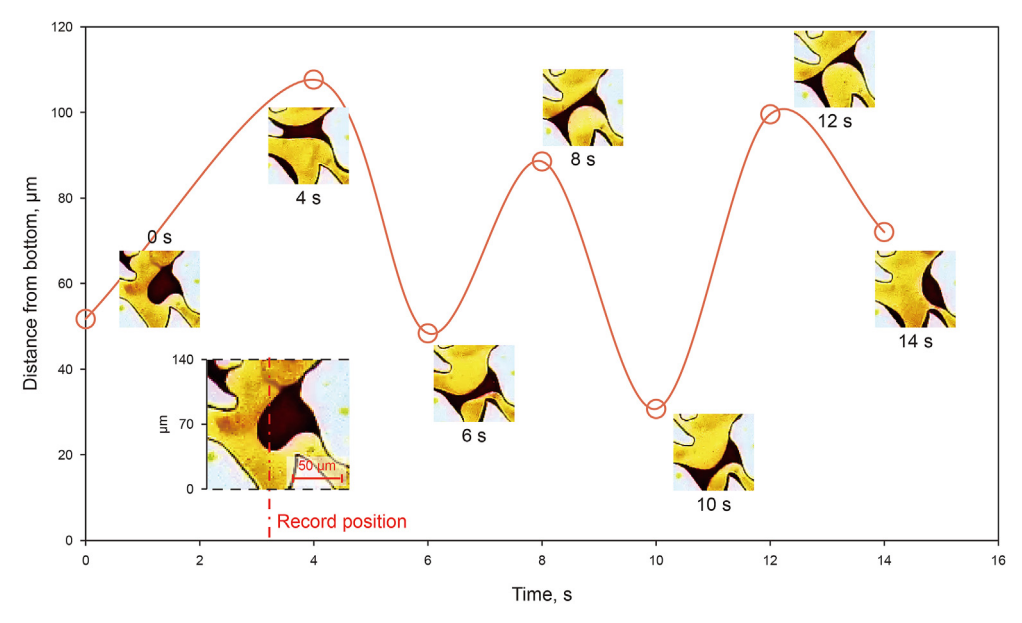


Fig. 21. The vertical movement trajectory of the membrane-like oil during the exploitation process.

the shear stress within the gas can cause a loss of pressure difference. According to Newton's shear law, this loss can be quantified; however, Hao et al. (2022) found that the shear stress-induced pressure loss in micro-visual experiments is significantly smaller than the pressure difference between the inlet and outlet of the model. Therefore, this loss is generally negligible.

$$F_{\rm d} = \Delta P \times d_{\rm p} T_{\rm o} \tag{17}$$

where $F_{\rm d}$ is the driving force provided by the pressure difference, N; $d_{\rm p}$ is the pore diameter, mm; $T_{\rm o}$ is the oil film thickness, mm. In the model of this paper, $T_{\rm o}$ is the depth of the microscopic model, which is 0.02 mm.

When gas displaces oil in the microscale space of the pore throat, the migration resistance is the capillary force generated on the gas—oil surface, for which Hao et al. (2022) provided a calculation method. For the research conditions of this paper, the formula for calculating this resistance is given by Eq. (18).

$$F_{\rm c} = \frac{2\sigma_{\rm o-g}(T_{\rm o} + L_{\rm a})\cos\theta}{T_{\rm o} \times L_{\rm a}} \times d_{\rm p} \times T_{\rm o}$$
 (18)

where $\sigma_{\text{0-g}}$ is the interfacial tension between CO₂ and oil, N/m; θ is the contact angle between CO₂ and oil on the chip surface, °; L_{a} is the arc length between CO₂ and the contact surface, mm.

When calculating the capillary force generated on the gas—oil surface, the treatment of the contact angle between CO_2 and oil on the chip surface is simplified. Usually, due to the irregular shape of the flow—solid, the contact angles at both ends are different, so the average value of the contact angles at both ends can be approximately taken to calculate the oil migration resistance. Thus, the boundary relationship for the exploitation of gas-driven oil in the pore space is obtained (Eq. (19)). When the driving force of the gas exceeds the migration resistance, the gas will push this part of the original oil into the next pore. According to the same mechanism mentioned above, the gas flow will repeatedly push the original oil forward, thereby achieving the purpose of exploiting residual oil.

$$F_{\rm c} = \frac{2\sigma_{\rm o-g}(T_{\rm o} + L_{\rm a})\cos\left(\frac{\theta_{\rm 1} + \theta_{\rm 2}}{2}\right)}{T_{\rm o} \times L_{\rm a}} \times d_{\rm p} \times T_{\rm o}$$
(19)

where θ_1 and θ_2 are the contact angles between CO₂ and oil at both ends of the chip surface, $^{\circ}$.

Overall, with periodic shutdown measures for production and injection wells, oil recovery rates significantly increase with the number of injection—production cycles, especially in the second and third cycles. Injection—production coupling technology

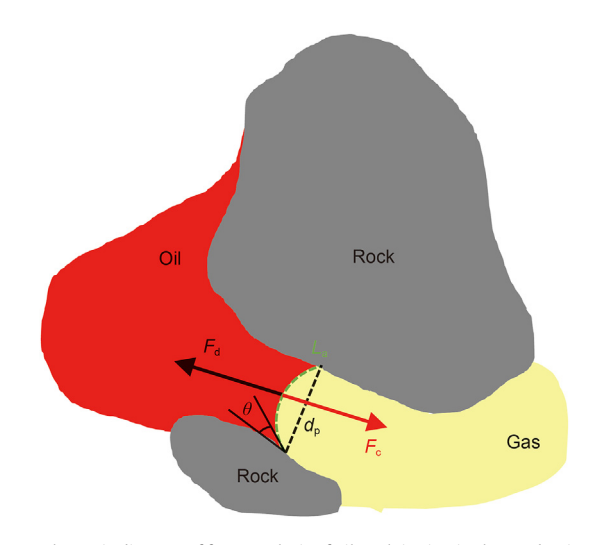


Fig. 23. Schematic diagram of force analysis of oil exploitation in the production stage.

optimizes the rhythm of injection and production in each cycle, allowing the expansion and migration mechanisms of residual oil to be fully utilized. Especially in the third and fourth cycles, porous residual oil is effectively dispersed and converted into membrane and columnar oils, thus reducing its proportion. This mechanism is enhanced through dynamic injection—production control in SCI, further improving CO₂ oil recovery efficiency. During shut-in period in each cycle, the dissolution and expansion effect of CO₂ provides additional elastic energy to the crude oil. This energy is released during subsequent production, driving the mobilization of residual oil. Injection—production coupling technology, through periodic adjustment of injection and production, fully utilizes this energy accumulation effect, thereby enhancing the overall energy efficiency of the CO₂ oil recovery process.

4. Conclusions

This study conducted extensive experimental work using microscopic techniques to explore CO₂-EOR and sequestration mechanisms under various injection—production modes. The effects of different methods on residual oil were analyzed, providing robust theoretical support for optimizing CO₂ injection and enhancing oil recovery during injection—production coupling. A stress analysis of the residual oil mobilization process during the injection—soak—production stages was also performed, elucidating the mechanical mechanisms of CO₂-EOR under different modes. The main conclusions based on our experimental results are:

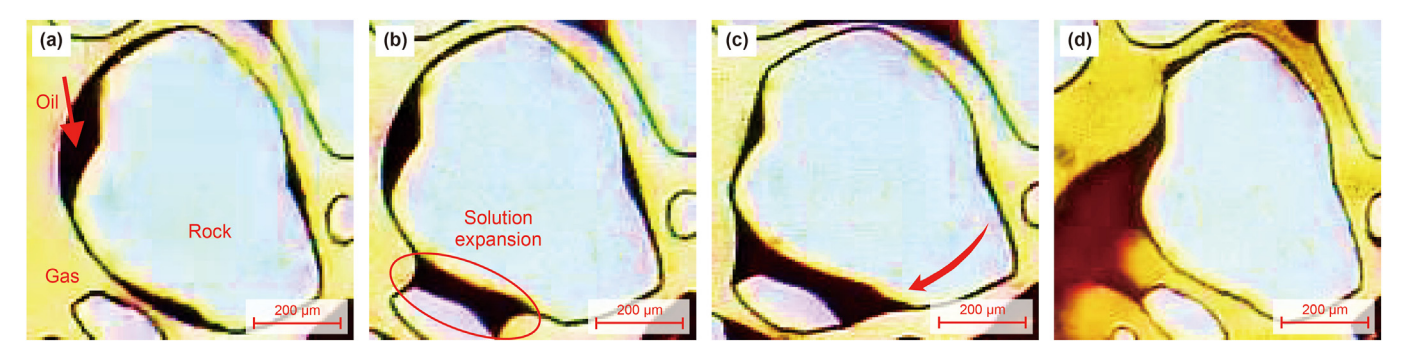


Fig. 22. Residual oil expansion—migration process: (a) initial distribution state before gas-oil soaking, (b) expansion due to oil dissolution, (c) migration and aggregation of residual oil in the same matrix, (d) residual oil being exploited in the production stage.

- (1) In the early stages of synchronous injection—production, there was no distinct interface between CO₂ and oil, indicating near-miscible displacement. Black heavy components were observed. As gas injection continued, CO₂ extraction became more pronounced near the injection point, leading to a clearer oil—gas interface and indicating a transition to immiscible displacement dominance.
- (2) Compared to CGI, the asynchronous injection—production mode resulted in a 6.58% increase in microscopic oil recovery rate. However, increasing displacement rates under the AIP mode did not significantly improve recovery rates. Under AIP, columnar and porous residual oil decreased by 6.75% and 4.84%, respectively, compared to CGI.
- (3) The AIP mode caused significant changes in the pressure field, enhancing CO₂ sweep efficiency. During the soak phase, membrane oil migrates due to adhesive forces, accumulating to form cluster and column oil. However, prolonged CO₂—oil contact may lead to the deposition of heavy components that block small pores, negatively impacting CO₂–EOR.
- (4) Compared to CGI, the SCI mode resulted in a 13.77% increase in microscopic recovery rate, and a 7.19% increase compared to AIP. The proportion of residual porous oil decreased by 7.1% and 12.8% under AIP and SCI modes, respectively, and columnar residual oil decreased by 6.8% under the HAIP mode.
- (5) When CO₂ dissolves into the residual oil within the pore throats, the crude oil volume expands, displaying a linear increase in the dynamic expansion coefficient. Under SCI mode, membrane oil exhibits filamentous flow and Kármán vortex patterns due to shear forces from the gas flow. Columnar oil is carried away by CO₂ gas flow, and continuous porous oil disperses into columnar and membrane oil. Additionally, dissolved and expanded oil aggregates and grows under adhesion forces at the oil—solid interface, aiding in its subsequent mobilization by CO₂.

This study constructed a microscopic simulation model based on cast thin-section images of geological cores. After pore connectivity processing, the pore sizes of the model tend to be larger compared to the actual sizes. Additionally, since the cast thin sections are single-layer images, the cutting position limitations mean that some pore images do not fully reflect the actual pore shapes and sizes. Therefore, in future research, we will explore constructing microscopic models based on three-dimensional pore connectivity scans of geological cores to better represent the actual geological conditions. On the other hand, this study attempted a theoretical mechanical analysis of the microscopic phenomena during the injection-production coupling process. However, due to current experimental conditions and the lack of certain measurement parameters, it is not feasible to use these equations for practical calculations. Therefore, the mechanical analysis remains at a theoretical level. Future work will involve developing and improving equipment, and integrating multidisciplinary technologies to obtain relevant experimental parameters to support subsequent theoretical calculations. Additionally, theoretical simulation methods will be employed to fit related experimental phenomena, in an attempt to conduct a comprehensive analysis of the force field changes during this process.

CRediT authorship contribution statement

Zheng Chen: Writing — original draft, Formal analysis, Investigation. **Yu-Liang Su:** Writing — review & editing, Funding acquisition, Conceptualization, Data curation. **Lei Li:** Funding acquisition, Methodology, Writing — review & editing. **Yong-Mao Hao:**

Supervision, Methodology, Validation. **Wen-Dong Wang:** Project administration, Resources. **Chui-Xian Kong:** Visualization, Writing — review & editing.

Declaration of competing interest

The authors declare that they have no known competing financial interests or personal relationships that could have appeared to influence the work reported in this paper.

Acknowledgments

This work was supported by the National Natural Science Foundation of China (Nos. 52374064, 51974347, 52474072) and the Shandong Provincial Universities Youth Innovation and Technology Support Program (2022KJ065).

References

- Ahmadi, M.A., Pouladi, B., Barghi, T., 2016. Numerical modeling of CO₂ injection scenarios in petroleum reservoirs: application to CO₂ sequestration and EOR. J. Nat. Gas Sci. Eng. 30, 38–49. https://doi.org/10.1016/j.jngse.2016.01.038.
- AL-khulaidi, G., Sun, Y., Alareqi, A.G., et al., 2024. Review on carbon capture, utilization, and storage for enhancing gas recovery. Energy Fuels. 38 (10), 8355–8384. https://doi.org/10.1021/acs.energyfuels.3c05211.
- Alam, M.M.M., Hassan, A., Mahmoud, M., et al., 2022. Dual benefits of enhanced oil recovery and CO₂ sequestration: the impact of CO₂ injection approach on oil recovery. Front. Energy Res. 10, 877212. https://doi.org/10.3389/ fenrg.2022.877212.
- Askarova, A., Mukhametdinova, A., Markovic, S., et al., 2023. An overview of geological CO₂ sequestration in oil and gas reservoirs. Energies 16 (6), 2821. https://doi.org/10.3390/en16062821.
- Chanson, H., 2009. Turbulent air—water flows in hydraulic structures: dynamic similarity and scale effects. Environ. Fluid Mech. 9, 125–142. https://doi.org/ 10.1007/s10652-008-9078-3.
- Chen, H., Liu, X.L., Zhang, C., et al., 2022a. Effects of miscible degree and pore scale on seepage characteristics of unconventional reservoirs fluids due to supercritical CO₂ injection. Energy 239, 122287. https://doi.org/10.1016/ j.energy.2021.122287.
- Chen, Z., Li, L., Su, Y.L., et al., 2024. Investigation of CO₂-EOR and storage mechanism in Injection-Production coupling technology considering reservoir heterogeneity. Fuel 368, 131595. https://doi.org/10.1016/j.fuel.2024.131595.
- Chen, Z., Su, Y.L., Li, L., et al., 2022b. Characteristics and mechanisms of supercritical CO₂ flooding under different factors in low-permeability reservoirs. Petrol. Sci. 19 (3), 1174–1184. https://doi.org/10.1016/j.petsci.2022.01.016.
- Cho, J., Min, B., Kwon, S., et al., 2021. Compositional modeling with formation damage to investigate the effects of CO₂—CH₄ water alternating gas (WAG) on performance of coupled enhanced oil recovery and geological carbon storage. J. Petrol. Sci. Eng. 205, 108795. https://doi.org/10.1016/j.petrol.2021.108795.
- Cui, M.L., Wang, R., Lv, C.Y., et al., 2017. Research on microscopic oil displacement mechanism of CO₂ EOR in extra-high water cut reservoirs. J. Petrol. Sci. Eng. 154, 315–321. https://doi.org/10.1016/j.petrol.2017.04.006.
- Davoodi, S., Al-Shargabi, M., Wood, D.A., et al., 2022. Experimental and field applications of nanotechnology for enhanced oil recovery purposes: a review. Fuel 324. 124669. https://doi.org/10.1016/i.fuel.2022.124669.
- Ding, M.C., Yuan, F.Q., Wang, Y.F., et al., 2017. Oil recovery from a CO₂ injection in heterogeneous reservoirs: the influence of permeability heterogeneity, CO₂-oil miscibility and injection pattern. J. Nat. Gas Sci. Eng. 44, 140–149. https://doi.org/10.1016/j.jngse.2017.04.015.
- Dudek, J., Janiga, D., Wojnarowski, P., 2021. Optimization of CO₂-EOR process management in polish mature reservoirs using smart well technology. J. Petrol. Sci. Eng. 197, 108060. https://doi.org/10.1016/j.petrol.2020.108060.
- Durst, F., 2022. Fluid Mechanics: An Introduction to the Theory of Fluid Flows. Springer Berlin Heidelberg, pp. 239–266. https://doi.org/10.1007/978-3-662-63915-3_8.
- Guo, Y.H., Liu, F., Qiu, J.J., et al., 2022. Microscopic transport and phase behaviors of CO₂ injection in heterogeneous formations using microfluidics. Energy 256, 124524. https://doi.org/10.1016/j.energy.2022.124524.
- Hao, Y.M., Li, Z.F., Su, Y.L., et al., 2022. Experimental investigation of CO₂ storage and oil production of different CO₂ injection methods at pore-scale and core-scale. Energy 254, 124349. https://doi.org/10.1016/j.energy.2022.124349.
- Heller, V., 2017. Self-similarity and Reynolds number invariance in Froude modelling. J. Hydraul. Res. 55 (3), 293–309. https://doi.org/10.1080/00221686.2016.1250832.
- Hou, J., Zhao, L., Zhao, W.Q., et al., 2023. Evaluation of pore-throat structures of carbonate reservoirs based on petrophysical facies division. Front. Earth Sci. 11, 1164751. https://doi.org/10.3389/feart.2023.1164751.
- Huang, F., Huang, H.D., Wang, Y.Q., et al., 2016. Assessment of miscibility effect for CO₂ flooding EOR in a low permeability reservoir. J. Petrol. Sci. Eng. 145,

- 328-335. https://doi.org/10.1016/j.petrol.2016.05.040.
- Jiang, S.X., Li, Y.N., Wang, F., et al., 2022. A state-of-the-art review of CO₂ enhanced oil recovery as a promising technology to achieve carbon neutrality in China. Environ. Res. 210, 112986. https://doi.org/10.1016/j.envres.2022.112986.
- Kang, W.L., Zhou, B.B., Issakhov, M., et al., 2022. Advances in enhanced oil recovery technologies for low permeability reservoirs. Petrol. Sci. 19 (4), 1622–1640. https://doi.org/10.1016/j.petsci.2022.06.010.
- Khather, M., Saeedi, A., Myers, M.B., et al., 2019. An experimental study for carbonate reservoirs on the impact of CO₂-EOR on petrophysics and oil recovery. Fuel 235, 1019–1038. https://doi.org/10.1016/j.fuel.2018.08.094.
- Kumar, N., Verma, A., Ahmad, T., et al., 2023. Carbon capture and sequestration technology for environmental remediation: a CO₂ utilization approach through EOR. Geoenergy Sci. Eng. 212619. https://doi.org/10.1016/j.geoen.2023.212619.
- Li, D.C., Saraji, S., Jiao, Z.S., et al., 2021a. CO₂ injection strategies for enhanced oil recovery and geological sequestration in a tight reservoir: an experimental study. Fuel 284, 119013. https://doi.org/10.1016/j.fuel.2020.119013.
- Li, D.C., Saraji, S., Jiao, Z.S., et al., 2023a. An experimental study of CO₂ injection strategies for enhanced oil recovery and geological sequestration in a fractured tight sandstone reservoir. Geoenergy Sci. Eng. 230, 212166. https://doi.org/ 10.1016/j.geoen.2023.212166.
- Li, F., Luo, Y., Luo, X., et al., 2016. Experimental study on a new plugging agent during CO₂ flooding for heterogeneous oil reservoirs: a case study of Block G89-1 of Shengli oilfield. J. Petrol. Sci. Eng. 146, 103–110. https://doi.org/10.1016/ i.petrol.2016.04.017.
- Li, H.B., Yang, Z.M., Li, R.S., et al., 2021b. Mechanism of CO₂ enhanced oil recovery in shale reservoirs. Petrol. Sci. 18 (6), 1788–1796. https://doi.org/10.1016/ j.petsci.2021.09.040.
- Li, H., 2023. Advancing "carbon peak" and "carbon neutrality" in China: a comprehensive review of current global research on carbon capture, utilization, and storage technology and its implications. ACS Omega 8 (45), 42086–42101. https://doi.org/10.1021/acsomega.3c06422.
- Li, L., Zhang, D., Su, Y.L., et al., 2024. Microfluidic insights into CO₂ sequestration and enhanced oil recovery in laminated shale reservoirs: post-fracturing interface dynamics and micro-scale mechanisms. Adv. Geo-Energy Res. 13 (3), 203–217. https://doi.org/10.46690/ager.2024.09.06.
- Li, L., Zhou, X.M., Wang, R., et al., 2023b. Microscopic experiment study on mechanisms of oil-gas interaction and CO₂-surfactant flooding with different temperatures and pressures. J. CO₂ Util. 69, 102389. https://doi.org/10.1016/i.icou.2022.102389.
- Li, Z.Y., Tan, H.Q., Li, L.X., et al., 2019. Research and application of injection-production coupling technology for enhancing oil recovery in reservoirs at later stage of polymer flooding. Petrol. Geology Recovery Effic. 26 (6), 115–121. https://doi.org/10.13673/j.cnki.cn37-1359/te.2019.06.015.
- Lin, C., Kao, M.J., Yang, J., et al., 2021. Similarity and Froude number similitude in kinematic and hydrodynamic features of solitary waves over horizontal bed. Processes 9 (8), 1420. https://doi.org/10.3390/pr9081420.
- Liu, S.Y., Ren, B., Li, H.Y., et al., 2022. CO₂ storage with enhanced gas recovery (CSEGR): a review of experimental and numerical studies. Petrol. Sci. 19 (2), 594–607. https://doi.org/10.1016/j.petsci.2021.12.009.
- Liu, X.L., Chen, H., Chen, Z.H., et al., 2024. Study on characterization and distribution of four regions of tight sandstone condensate gas reservoirs in the depletion development process. Fuel 358, 130267. https://doi.org/10.1016/j.fuel.2023.130267.
- Lu, H.W., Huang, F., Jiang, P.X., et al., 2021. Exsolution effects in CO₂ huff-n-puff enhanced oil recovery: water-Oil-CO₂ three phase flow visualization and measurements by micro-PIV in micromodel. Int. J. Greenh. Gas Control 111, 103445. https://doi.org/10.1016/ji.jiggc.2021.103445.
- Luo, J.S., Hou, Z.M., Feng, G.Q., et al., 2022. Effect of reservoir heterogeneity on CO₂ flooding in tight oil reservoirs. Energies 15 (9), 3015. https://doi.org/10.3390/en15093015.
- Lv, Q.C., Zheng, R., Zhou, T.K., et al., 2022. Visualization study of CO₂-EOR in carbonate reservoirs using 2.5D heterogeneous micromodels for CCUS. Fuel 330, 125533. https://doi.org/10.1016/j.fuel.2022.125533.
- Mahdavi, S., Jalilian, M., Dolati, S., 2024. Review and perspectives on CO₂ induced asphaltene instability: fundamentals and implications for phase behaviour, flow assurance, and formation damage in oil reservoirs. Fuel 368, 131574. https:// doi.org/10.1016/j.fuel.2024.131574.
- Menefee, A.H., Ellis, B.R., 2020. Regional-scale greenhouse gas utilization strategies for enhanced shale oil recovery and carbon management. Energy Fuels. 34 (5), 6136–6147. https://doi.org/10.1021/acs.energyfuels.0c00562.
- Qian, K., Yang, S.L., Dou, H.E., et al., 2018. Experimental investigation on microscopic residual oil distribution during CO₂ Huff-and-Puff process in tight oil reservoirs. Energies 11 (10), 2843. https://doi.org/10.3390/en11102843.
- Ryutov, D., Drake, R., Kane, J., et al., 1999. Similarity criteria for the laboratory simulation of supernova hydrodynamics. Astrophys. J. 518 (2), 821. https://doi.org/10.1086/307293

Sadeghnejad, S., Enzmann, F., Kersten, M., 2021. Digital rock physics, chemistry, and biology: challenges and prospects of pore-scale modelling approach. Appl. Geochem. 131, 105028. https://doi.org/10.1016/j.apgeochem.2021.105028.

- Shchipanov, A., Kollbotn, L., Encinas, M., et al., 2022. Periodic CO₂ injection for improved storage capacity and pressure management under intermittent CO₂ supply. Energies 15 (2), 566. https://doi.org/10.3390/en15020566.
- Song, Z.J., Hou, J.R., Liu, X.C., et al., 2018a. Conformance control for CO₂-EOR in naturally fractured low permeability oil reservoirs. J. Petrol. Sci. Eng. 166, 225–234. https://doi.org/10.1016/j.petrol.2018.03.030.
- Song, Z.Y., Zhu, W.Y., Wang, X., et al., 2018b. 2-D pore-scale experimental investigations of asphaltene deposition and heavy oil recovery by CO₂ flooding. Energy Fuels 32 (3), 3194–3201. https://doi.org/10.1021/acs.energyfuels.7b03805.
- Su, Y.L., Zhang, X., Li, L., et al., 2022. Experimental study on microscopic mechanisms and displacement efficiency of N₂ flooding in deep-buried clastic reservoirs. J. Petrol. Sci. Eng. 208, 109789. https://doi.org/10.1016/j.petrol.2021.109789.
- Sugiyama, K., Sbragaglia, M., 2008. Linear shear flow past a hemispherical droplet adhering to a solid surface. J. Eng. Math. 62, 35–50. https://doi.org/10.1007/s10665-007-9185-z.
- Sun, L.T., Cui, C.Z., Wu, Z.W., et al., 2023. A mathematical model of CO₂ miscible front migration in tight reservoirs with injection-production coupling technology. Geoenergy Sci. Eng. 221, 211376. https://doi.org/10.1016/ i.geoen.2022.211376.
- Syah, R., Alizadeh, S., Nasution, M.K., et al., 2021. Carbon dioxide-based enhanced oil recovery methods to evaluate tight oil reservoirs productivity: a laboratory perspective coupled with geo-sequestration feature. Energy Rep. 7, 4697–4704. https://doi.org/10.1016/j.egyr.2021.07.043.
- Syed, F.I., Neghabhan, S., Zolfaghari, A., et al., 2020. Numerical validation of asphaltene precipitation and deposition during CO₂ miscible flooding. Petrol. Res. 5 (3), 235–243. https://doi.org/10.1016/j.ptlrs.2020.04.002.
- Tang, Y., Hou, C.X., He, Y.W., et al., 2023. Microscopic flow characteristics of immiscible CO₂ flooding and CO₂ foam flooding after water flooding in fractured porous media: a visual investigation. Transport Porous Media 149 (1), 117–145. https://doi.org/10.1007/s11242-023-01953-1.
- Wang, L., He, Y.M., Wang, Q., et al., 2020. Multiphase flow characteristics and EOR mechanism of immiscible CO₂ water-alternating-gas injection after continuous CO₂ injection: a micro-scale visual investigation. Fuel 282, 118689. https://doi.org/10.1016/j.fuel.2020.118689.
- Wang, Y.Y., Wang, X.G., Dong, R.C., et al., 2023. Reservoir heterogeneity controls of CO₂-EOR and storage potentials in residual oil zones: insights from numerical simulations. Petrol. Sci. 20 (5), 2879–2891. https://doi.org/10.1016/j.petsci.2023.03.023.
- Wang, R., Yuan, S.B., Wang, J., 2018. Mechanism of the injection-production coupling technique for complex fault-block oil reservoirs. Pet. Geol. Oilfield Dev. Daqing 37 (6), 38–42. https://doi.org/10.19597/j.issn.1000-3754.201712022.
- Wei, J.G., Zhou, X.F., Zhou, J.M., et al., 2021. Experimental and simulation investigations of carbon storage associated with CO₂ EOR in low-permeability reservoir. Int. J. Greenh. Gas Control 104, 103203. https://doi.org/10.1016/j.ijggc.2020.103203.
- Yao, J.Y., Yuan, W.J., Peng, X.L., et al., 2023. A novel multi-phase strategy for optimizing CO₂ utilization and storage in an oil reservoir. Energies 16 (14), 5289. https://doi.org/10.3390/en16145289.
- Yu, H.Y., Fu, W.R., Zhang, Y.P., et al., 2021. Experimental study on EOR performance of CO₂-based flooding methods on tight oil. Fuel 290, 119988. https://doi.org/ 10.1016/j.fuel.2020.119988.
- Yu, H.M., Yang, J.Q., Li, W.L., et al., 2024. Study on fluid phase behavior characteristics of low permeability reservoir under different CO₂ injection amounts. Energy Rep. 12, 2297–2305. https://doi.org/10.1016/j.egyr.2024.08.024.
- Zhang, K.Q., Jia, N., Li, S.Y., et al., 2019. Static and dynamic behavior of CO₂ enhanced oil recovery in shale reservoirs: experimental nanofluidics and theoretical models with dual-scale nanopores. Appl. Energy 255, 113752. https://doi.org/ 10.1016/j.apenergy.2019.113752.
- Zhang, X., Su, Y.L., Li, L., et al., 2022a. Microscopic remaining oil initiation mechanism and formation damage of CO₂ injection after waterflooding in deep reservoirs. Energy 248, 123649. https://doi.org/10.1016/j.energy.2022.123649.
- Zhang, Y.L., Shi, L.T., Ye, Z.B., et al., 2022b. Experimental investigation of supercritical CO₂—rock—water interactions in a tight formation with the pore scale during CO₂—EOR and sequestration. ACS Omega 7 (31), 27291–27299. https://doi.org/10.1021/acsomega.2c02246.
- Zheng, W.K., Yang, Y., Lv, G.Z., 2021. EOR by injection-production coupling technique of CO₂ flooding. J. Xi'an Shiyou University: Nat. Sci. 36 (5), 77–82.
- Zhu, D., Li, B.F., Chen, L.K., et al., 2024. Experimental investigation of CO₂ foam flooding-enhanced oil recovery in fractured low-permeability reservoirs: corescale to pore-scale. Fuel 362, 130792. https://doi.org/10.1016/j.fuel.2023.130792.